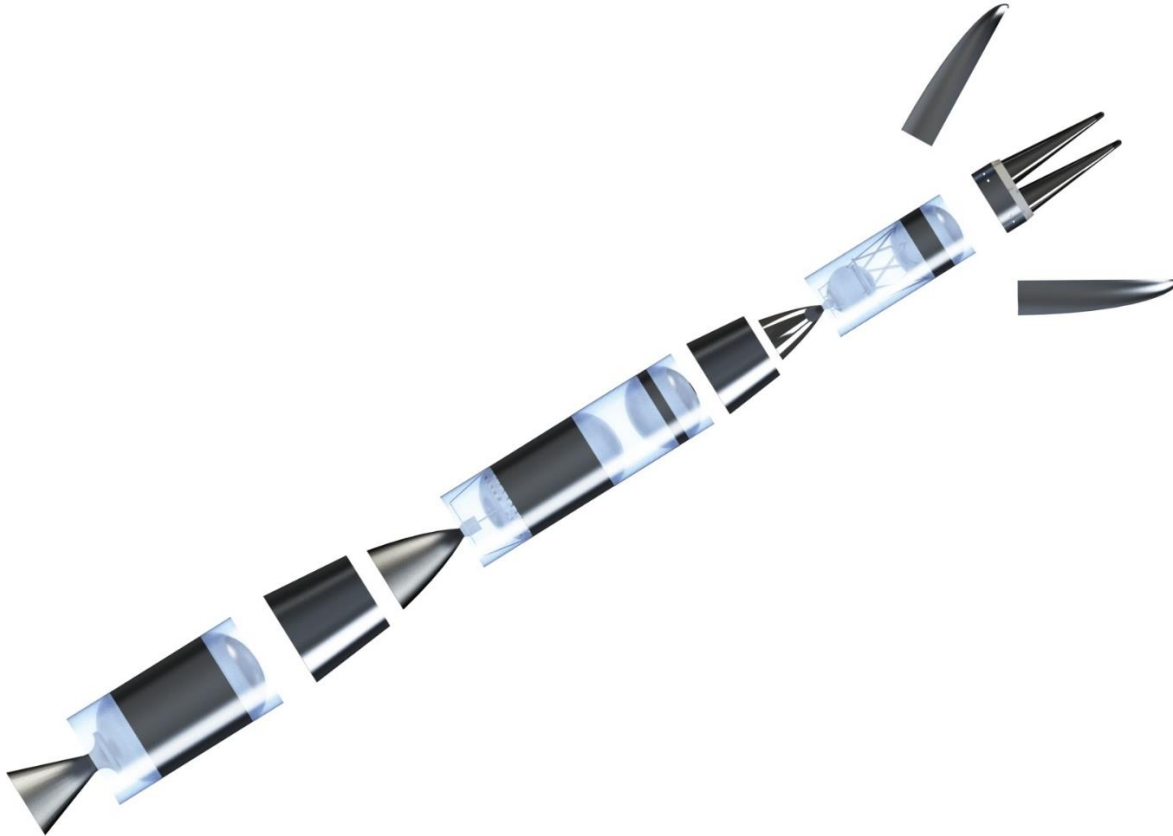


Project Fenrir

Proposal for the Replacement of the Minuteman-III ICBMs



Submitted by:

Team: Stripe Aerospace

Colby Truong

John Clements

Edgar Diaz

Eric Gonzalez

Rushi Patel

Courtney Sorenson

Nolan Wells

Faculty Advisor

Dr. Donald Edberg

California State Polytechnic University, Pomona
Department of Aerospace Engineering

3801 W Temple Ave
Pomona, CA 91768

May 10th, 2019

AIAA Graduate Team Missile Systems Design Competition – Long Range Strategic Missile



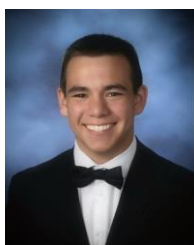
Colby Truong
Team Lead, Aerothermodynamics, Trajectory

AIAA Member No: #761762



Dr. Donald Edberg
Faculty Advisor

AIAA Member No: #022972-00



John Clements
Logistics & Operations

AIAA Member No: #983374



Edgar Diaz
Vehicle Design, CAD

AIAA Member No: #983827



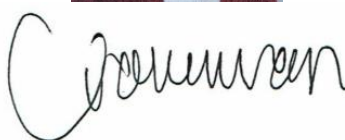
Eric Gonzalez
Deputy Lead, Propulsion

AIAA Member No: #834530



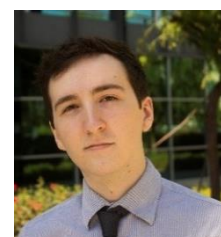
Rushi Patel
Trajectory, Design
Optimization

AIAA Member No: #983283



Courtney Sorenson
Guidance, Navigation, &
Controls

AIAA Member No: #983829



Nolan Wells
Structures

AIAA Member No: #983027

Executive Summary

The need has risen to replace the United States' inventory of the aging Minuteman-III intercontinental ballistic missiles (ICBMs) in order for the nation to maintain a credible nuclear deterrent. Stripe Aerospace presents Project Fenrir as a response to the Long Range Strategic Missile request for proposal (RFP) sponsored by the American Institute of Aeronautics and Astronautics (AIAA) Missile Systems Technical Committee (MSTC).

Following the requirements set by the RFP, the proposed missile will be capable of delivering two 1000 lb_m independently guided warheads to targets of interest from a maximum distance with an objective range of 10,000 nmi (threshold of 7,000 nmi). Additionally, the missile must be capable of storage for up to 20 years without maintenance.

Two system architectures were considered: a conventional ballistic missile using a post boost vehicle to deploy independent reentry vehicle (RV) and missile launched hypersonic glide vehicles (HGV). Using risk and technology development as the main factors for architecture downselection, the conventional ballistic missile design was chosen due to having mature technology that are based on the Minuteman-III. The ability to use the HGV is still under consideration; however, it is not the primary focus of the design.

The missile is sized to fit inside current Minuteman-III silos, thus not requiring any major changes to the launch platform. It uses three stages: an APCP solid first stage, an MMH/N₂O₄ second stage, and a JP-10/98% H₂O₂ third stage. The missile is designed with H₂O₂ monopropellant post boost vehicle that can carry up to two RVs. The proposed system is expected to cost \$111.9 billion and achieve the 2029 initial operational capability with manufacturing of the final product starting in late 2026. The proposed system meets all requirements laid out by the RFP.

Table of Contents

1	Introduction.....	1
1.1	Purpose and Requirements for Vehicle Design.....	1
2	Preliminary Considerations.....	2
2.1	Relevant Treaties Affecting ICBM Design.....	2
2.2	Launch Platform Integration	3
2.3	Target Engagement	5
2.4	Range Requirement Assessment	6
3	System Architectures	8
3.1	Assessment of Two Candidate Architectures.....	8
3.2	Concept of Operations.....	9
3.3	Selected Architecture	11
4	Vehicle Design and Sizing.....	13
4.1	ΔV Estimation	14
4.2	Propellant Selection.....	15
4.3	Launch Vehicle Family Sizing Analysis	17
4.4	Inboard Profile Design Process	18
4.4.1	Tank Design	18
4.4.2	Solid Motor/Liquid Engine Sizing.....	19
4.4.3	Pump Sizing	22

4.4.4	Post-Boost Vehicle.....	23
4.4.5	Fairing.....	24
4.4.6	Re-entry Vehicle.....	25
4.4.7	Separation Devices.....	26
4.4.8	Scale Drawing and Mass Properties.....	26
4.4.9	CAD Model Views.....	29
5	Trajectory.....	31
5.1	Ballistic Trajectory Approach and Modelling.....	32
5.2	Optimized Trajectory to Meet Requirements.....	35
5.2.1	Ascent (Boost) Trajectory.....	36
5.2.2	Reentry Trajectory.....	39
5.2.3	Overall Trajectory Results.....	41
5.3	Reentry Heating.....	43
5.4	Circular Error Probable.....	47
6	Structural Analysis.....	49
6.1	Ground Loads.....	49
6.2	Max q Data.....	51
6.3	Calculation of Load Distributions.....	52
6.4	Stress Analysis.....	57
7	Guidance, Navigation, and Controls.....	58

7.1	Initial Stability Estimation	58
7.2	Implementation of PID Controller	59
7.3	Frequency Analysis	62
8	Hypersonic Glide Vehicle Design and Analysis.....	63
8.1	Waverider Design.....	63
8.1.1	Geometric Relations.....	65
8.2	HGV Trajectory.....	67
9	System Level Considerations.....	71
9.1	Operations	71
9.2	System Maintenance	71
9.3	End of Mission Concepts	72
9.4	Manufacturing	72
9.5	Reliability/Redundancy Analysis.....	73
9.6	Cost Analysis.....	76
9.7	Program Timeline.....	78
10	Compliance Matrix	79
11	Summary and Conclusions	81
	References.....	83

List of Figures

Figure 2.1: Summary of treaties.....	3
Figure 2.2: Minuteman-III silo dimensions	5
Figure 3.1: Architecture #1 Model.....	8
Figure 3.2: Architecture #2 Model with Glider	9
Figure 3.3: Architecture #1 ConOps.....	10
Figure 3.4: Architecture #2 ConOps.....	11
Figure 4.1: Ballistic trajectory geometry	14
Figure 4.2: Decomposition of Hydrogen Peroxide	16
Figure 4.3: Final Tank Dimensions for Architecture 1	19
Figure 4.4: Stage 1 Nozzle Geometry.....	21
Figure 4.5: Stage 2 Engine Geometry.....	21
Figure 4.6: Stage 3 Engine Geometry.....	22
Figure 4.7: Architecture 1 Pump Requirements	23
Figure 4.8: Post-Boost Vehicle Design.....	24
Figure 4.9: Clam shell release fairing design.....	25
Figure 4.10: RV design and dimensions	25
Figure 4.11: Scale Drawing of Vehicle.....	27
Figure 4.12: Mass Breakdown of Vehicle	27
Figure 4.13: Diagram with CM and CP	28
Figure 4.14: Side and bottom view of ICBM	29
Figure 4.15: ICBM configuration	30
Figure 5.1: Graphical representation of Coordinate System for Equations of Motion [13]	33

Figure 5.2: Titan II Drag Model (Provided by Faculty Advisor)	34
Figure 5.3: Overview of trajectory optimization	35
Figure 5.4: Ascent Trajectory Parameters vs. Time	37
Figure 5.5: Time history of vehicle weight and propellant mass flow rate during boost	38
Figure 5.6: Time history of thrust and drag during boost ascent trajectory.....	38
Figure 5.7: Time history of parameters for reentry trajectory	40
Figure 5.8: Time history of RV lift and drag forces	40
Figure 5.9: Time history of parameters for entire trajectory	42
Figure 5.10: Time history of altitude and range for the entire trajectory	42
Figure 5.11: 3D Overview of Trajectory	43
Figure 5.12: Ground Track of Trajectory	43
Figure 5.13: Stagnation point heat flux plotted against altitude	45
Figure 5.14: Stagnation temperature and heat flux versus time.....	46
Figure 5.15: Temperature distribution of RV surface at select times into reentry flight.....	46
Figure 5.16: CEP results for 500 simulations	48
Figure 6.1: Ground Axial Load Distribution	51
Figure 6.2: Max-q Shear Load Distribution.....	55
Figure 6.3: Max-q Moment Distribution	56
Figure 6.4: Max-q Axial Load Distribution.....	56
Figure 7.1: Root locus with no controller implemented	59
Figure 7.2: Root locus with PID controller implemented.....	60
Figure 7.3: System response to step input	61
Figure 7.4: Block diagram for system with a PID controller.....	61

Figure 7.5: Detailed block diagram of sensor-actuator system.....	62
Figure 8.1: Streamline tracing to form the compression surface of a waverider [17]	64
Figure 8.2: Optimization process to design a viscous optimized waverider. Original illustration from [23]	65
Figure 8.3: MATLAB output of waverider shape in inches	66
Figure 8.4: 3-view diagram of HGV CAD model	67
Figure 8.5: Time history of HGV trajectory parameters.....	69
Figure 8.6: Ground track of the HGV trajectory.....	70
Figure 9.1: Manufacturing Plan	73
Figure 9.2: Program Timeline.....	78

List of Tables

Table 1.1: Summary of key requirements.....	1
Table 4.1: Specific impulses of possible propellants.....	15
Table 4.2 Mass Breakdown of Selected Architecture.....	18
Table 4.3: Summary of Motor/Engine Parameters	21
Table 4.4: Intertanks, Interstages, and extra accommodation dimensioning.....	26
Table 4.5: Mass Properties of Vehicle.....	28
Table 5.1: Ascent Trajectory Analysis Results.....	36
Table 5.2: Initial conditions for reentry trajectory.....	39
Table 5.3: Impact parameters for RVs.....	41
Table 5.4: Key results for entire trajectory	41
Table 5.5: Values for estimating hypersonic aerodynamic heating.....	44
Table 5.6: Summary of CEP tolerances for RV initial conditions.....	48
Table 6.1: Ground Axial Loads	50
Table 6.2: Max-q Parameters	51
Table 6.3: Vehicle Max-q Flight Loads.....	53
Table 6.4: Total Shear, Axial, and Moment Distributions.....	54
Table 6.5: Stress Analysis Summary	57
Table 8.1: Initial conditions for HGV trajectory	68
Table 8.2: HGV maneuvers	68
Table 8.3: Impact parameters from HGV trajectory.....	69
Table 9.1: Key part reliability analysis.....	74
Table 9.2: Derived subsystem reliability	75

Table 9.3: General subsystem reliability analysis.....	76
Table 9.4: Cost Estimation Breakdown	77
Table 10.1: Compliance Matrix	79

List of Abbreviations

AIAA	American Institute of Aeronautics and Astronautics
AP	Ammonium Perchlorate
CAD	Computed aided design
CEA	Chemical Equilibrium with Applications
CEP	Circular Error Probable
ConOps	Concept of Operations
GPS	Global Positioning System
HGV	Hypersonic Glide Vehicle
ICBM	Intercontinental Ballistic Missile
IMU	Inertial Measurement Unit
IOC	Initial Operational Capability
MMH	Monomethyl Hydrazine
PBAN	Polybutadiene Acrylonitrile
PBV	Post boost vehicle
PID	Proportional-Integral-Derivative
RFP	Request for proposal
RV	Reentry Vehicle
STK	Systems Tool Kit
USAF	United States Air Force

1 Introduction

1.1 Purpose and Requirements for Vehicle Design

This proposal responds to the 2018-2019 Graduate Team Missile Systems Design Competition – Long Range Strategic Missile request for a replacement to the current ICBM fleet in the United States. The Minuteman III missiles were introduced in 1970 and now the country needs the next generation of ICBMs to remain a credible nuclear deterrent. The top-level system requirements are as follows:

Table 1.1: Summary of key requirements

Metric	Requirement
Payload	Capable of carrying a minimum of two, independently guided 1000 lb _m payloads with a 22 in diameter and 80 in length
Range	Maximum threshold distance of 7000 nmi, with an objective range of 10000 nmi
Platform Integration	Compatible with existing Minuteman III silos for fixed launches or from a truck/train car for mobile launches
Storage and Handling	Safe storage of weapon system for a minimum of 20 years without maintenance
Accuracy	Circular Error Probable (CEP) of each payload shall be a maximum of 100 ft (objective), 150 ft (threshold) with a footprint of 100 nmi between impact points
Trajectory	Objective payload deployment time of 60 minutes, threshold of 90 minutes
Schedule	Development begins October 2020; initial operational capability occurring no later than December 2029

2 Preliminary Considerations

Nomenclature

Symbols

A	=	Cross sectional area
d	=	Penetration depth
N	=	Nose coefficient
S	=	Penetrability of target
V	=	Impact velocity
W	=	Weight of reentry vehicle

2.1 Relevant Treaties Affecting ICBM Design

As to not design something that would impose on international treaties all current treaties were studied. Not only does being knowledgeable of relevant treaties prevent a missile design from being unusable, many treaties have affected the manufacturing and testing process of these strategic missiles.

Starting with one of the most impactful and relevant was the Treaty of the Non-Proliferation of Nuclear Weapons crafted by the International Community. This treaty shaped many future treaties stating that the countries participating “pursue good-faith negotiations on measures relating to cessation of the nuclear arms race...”. A practice Stripe Aerospace would like to follow.

For manufacturing and deployment options the New Start treaty between United States and Russia limits the total number of ICBMs and warheads each country can have in their arsenal. A planned production or backlog of units will be limited by this treaty. New Start also states that Russia must be made aware of where our active nuclear weapons are stored. This was the driving decision in not choosing a mobile launcher. As a loaded mobile launcher location must always send its location out, it loses its stealth advantage.

For testing plans the Treaty Banning Nuclear Tests in the Atmosphere, in Outer Space, and Under Water written by the United Nations constrains how and where ICBM tests can happen.

This treaty is focused around public safety and the preservation of wildlife. Any planned demonstration of Strip Aerospace’s product will confine to a testing plan which abides by the rules listed above. A summary of these treaties can be seen in Figure 2.1.

<p>International Community</p>	<p>Treaty on the Non-Proliferation of Nuclear Weapons</p>	<p>1) Pledge not to transfer nuclear explosive devices to any recipient, assist, encourage or induce any non-nuclear-weapon state in the manufacture or acquisition of a nuclear weapon.</p> <p>2) To pursue good-faith negotiations on measures relating to cessation of the nuclear arms race, nuclear disarmament, and complete disarmament.</p>	
<p>United States & Russian</p>	<p>New Start</p>	<p>Type</p>	<p>Limited to</p>
		<p>Deployed Missiles and Bombers</p>	<p>700</p>
		<p>Total Launchers</p>	<p>800</p>
		<p>Deployed Warheads</p>	<p>1,550</p>
<p>United Nations</p>	<p>Treaty Banning Nuclear Tests in the Atmosphere, in Outer Space and Under Water</p>	<p>Prohibit, prevent, and abstain from carrying out nuclear weapons in the atmosphere, outer space, under water, or in any other environment if such explosions cause radioactive debris to be present outside the territorial limits of the State that conducts an explosion; to refrain from causing, encouraging, or in any way participating in, a nuclear weapon test explosion, anywhere which would take place in any of the above-described environments.</p>	

Figure 2.1: Summary of treaties

2.2 Launch Platform Integration

The launch vehicle needs to be capable of launch from one of two means: from existing Minuteman III silos for a fixed launch or from a truck/ train car for mobile launches. Based off current worldwide configurations a feasibility analysis was done on the mobile launch platform for its advantages and disadvantages. It was discovered that the cost of a mobile launcher would range anywhere from \$30 B to \$80 B. [1] Based off previous designs of mobile launch platforms, it is estimated that the individual vehicle weight would be upwards of 100 T. The weight of the launcher and vehicle combined would limit greatly where the mobile platform could access.

Transportation is not only limited by safe access due to the weight, but also by the security risks posed when transportation is mixed with civilian traffic and population centers. This restricts the range of where these mobile launchers can realistically travel. Lastly, the New START Treaty between the United States and Russia restricts deployed mobile launchers strictly to ICBM bases. This alone makes it so that a mobile platform of any kind is highly limited in its range so much so that it was determined there is minimal to no benefit in considering a mobile launch platform for the design. [2]

To comply with the requirements, the vehicle must then be compatible with current Minuteman III silos as a launch platform. Through research the dimensions of current silos were determined so that vehicle sizing could be done to ensure an appropriate fit. Based off the Delta – 09 launch facility in South Dakota, the usable diameter of the silo is 12.1 ft and the height from the bottom of the launch tube to the top of the launcher door is 80.4 ft as shown in Figure 2.2. Assuming no modifications to the silo, the maximum launch vehicle length could be 74.5 ft and the maximum diameter could be 11.5 ft. These dimensions and limitation assumptions were used to size the iterations of the launch vehicle to integrate it with the current silos. [3]

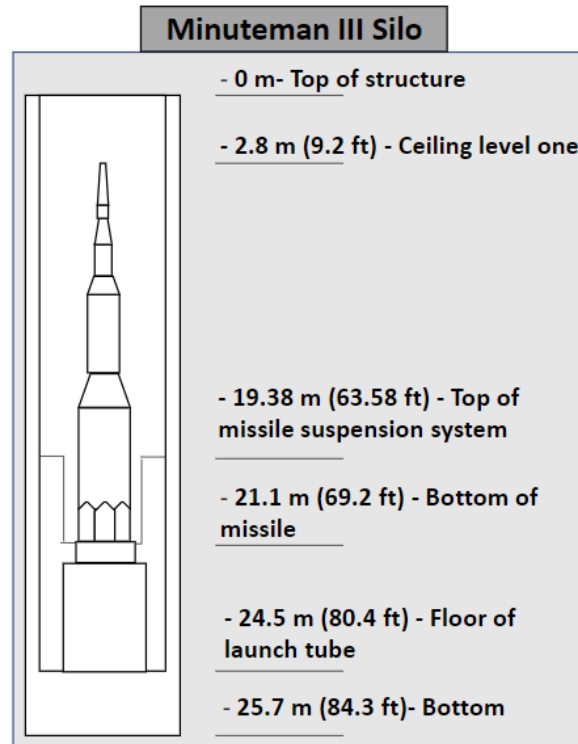


Figure 2.2: Minuteman-III silo dimensions

2.3 Target Engagement

Based on the research done by Sandia National Laboratories, the optimal penetration depth for a warhead was found to be 9.8 ft. (3 m.) for weapon survivability and maximum ground shock coupling. [4] Assuming a hard target such as concrete and given that the nuclear warhead has a 300 kt yield, the following equation was manipulated to determine the impact velocity necessary to achieve the desired penetration depth:

$$d = 0.00178SN\left(\frac{W}{A}\right)^{0.7}(V - 100) \quad (2.1)$$

After calculating the nose performance coefficient based on the warheads' geometry and the cross-sectional area of the warhead, then inputting all given values, the necessary impact velocity was found to be 1180 fps (360 m/s). [5] This optimized impact velocity allows for reentry trajectory calculations to ensure our vehicle can eliminate deeply buried and hardened

targets or hold them at risk of destruction. The RV will also houses a height-of-burst (HOB) sensor for soft targets for optimal altitude detonation. The system will be capable of multiple HOB settings to achieve mission success while minimizing collateral damage and fallout where possible. The impact velocity requirement for target engagement was modeled into the launch-to-impact code to discover the most efficient trajectory considering aerodynamic loads & stresses, payload deployment time, and ground range.

2.4 Range Requirement Assessment

The objective ground range requirement was assessed using Systems Tool Kit (STK). All major locations of Minuteman III silos were incorporated, and the ground range measurement tool was used to visualize the 10,000 nautical mile ground range. Upon analysis, it was found that a range of 10,000 nautical miles was excessive and reducing the ground range requirement was appropriate. The original ground range and new ground range for a launch from Warren Air Force Base is shown in the Figure 2.4. Note that the region within the yellow circle cannot be targeted.

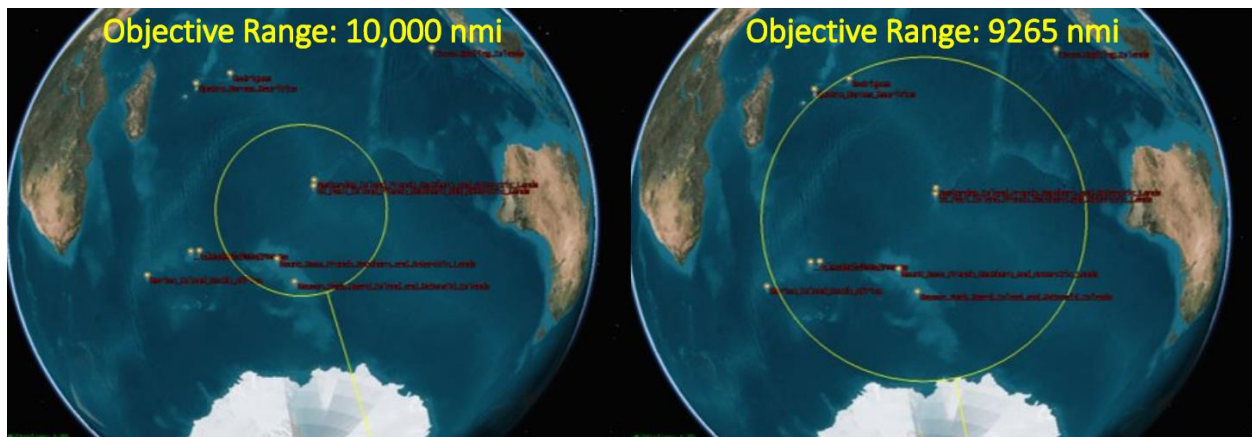


Fig. 2.4: Ground Range Analysis from Warren Air Force Base

As is evident from the Figure 2.4, the original ground range of 10,000 nautical miles resulted in a target in the middle of the Indian ocean. The ground range marker in Figure 2.4, which is indicated by the yellow circle, was expanded until it touched a major landmass which in

this case was Antarctica. This analysis was conducted for every major location known to have a Minuteman III silo location to determine the maximum reduction possible in ground range. The result of the analysis is tabulated in Table 2.4 below.

Table 2.4 Ground Range Analysis Results

LAUNCH LOCATION	CURRENT RANGE km, (nmi)	NEW RANGE km, (nmi)	ΔRANGE km, (nmi)	Percentage Diff (%)
Warren AFB, Wyoming	18,520 (10,000)	17,159 (9,265)	1,361 (735)	7.35
Minot AFB, North Dakota	18,520 (10,000)	17,990 (9,714)	530 (286)	2.86
Malmstrom AFB, Montana	18,520 (10,000)	17,779 (9,600)	741 (400)	4.00
Ellsworth AFB, South Dakota	18,520 (10,000)	17,501 (9,450)	1,019 (550)	5.50
Vandenberg AFB, California	18,520 (10,000)	18,411 (9,941)	109 (59)	0.59
Cape Canaveral AFS, Florida	18,520 (10,000)	18,520 (10,000)	0	0.00

Launching from Warren Air Force Base did indeed permit the maximum ground range reduction of 735 nmi. This was beneficial as it allowed for a relatively smaller ICBM which could be accommodated within the existing Minuteman III silos and satisfy the compatibility requirement.

3 System Architectures

3.1 Assessment of Two Candidate Architectures

To address the RFP, two independent system candidate architectures were designed. The first system architecture is the conventional ballistic missile. It was modeled after the Minuteman III to a certain degree. It utilized a solid first stage rocket motor with liquid second and third stages. This configuration houses a post boost vehicle (PBV) and reentry vehicles (RV) to deploy the warheads. This system follows the conventional ballistic trajectory and is compatible with the current Minuteman III silos. Figure 3-1 shows a model of architecture #1's concept.

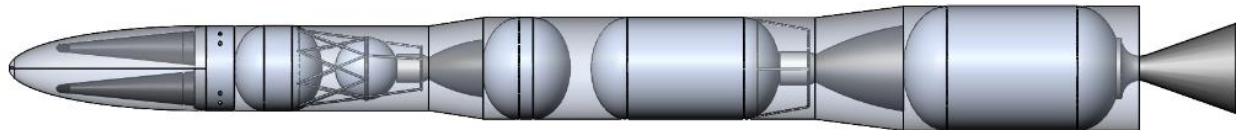


Figure 3.1: Architecture #1 Model

The second architecture is the hypersonic glide vehicle (HGV). This ICBM uses a solid first stage rocket motor and a hypergolic second stage to accelerate the hypersonic glide vehicle to hypersonic speeds. The hypersonic glide vehicle contains the warheads and is released in the upper atmosphere. The HGV is capable of midflight maneuvers for better targeting and avoiding interception. The possibility of a mobile launch configuration was also considered. Figure 3.2 shows a model of architecture #2 with glider.

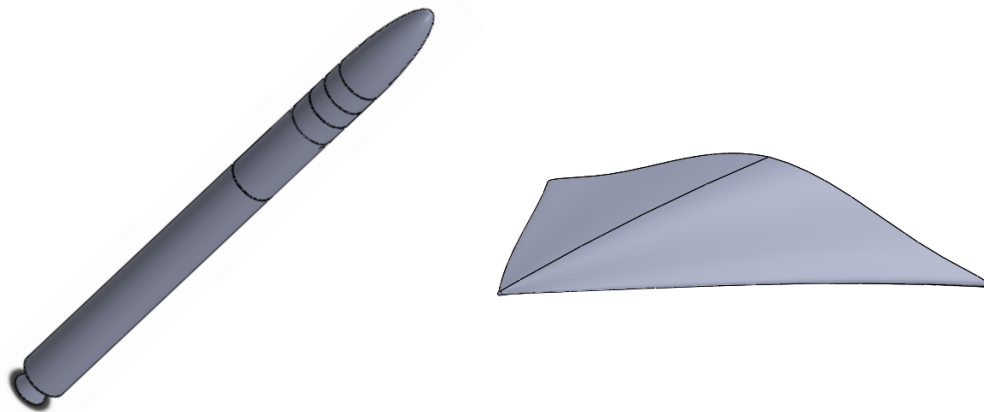


Figure 3.2: Architecture #2 Model with Glider

When assessing the viability of both architectures, several factors were taken into consideration. First, the maturity of the technology was assessed. Given the innovative use of a hypersonic glide, architecture 2 calls for more research and development. Additionally, the ease of redesign was considered, as iterative optimizations will be frequently required for the early stages of design.

3.2 Concept of Operations

The ICBM will follow conventional rocket staging similar to that of a heavy lift launch vehicle. The ICBM is specifically designed to meet the requirements while being able to launch out of the current Minuteman III silos. The concept of operations for architecture 1 is summarized in Figure 3.3.

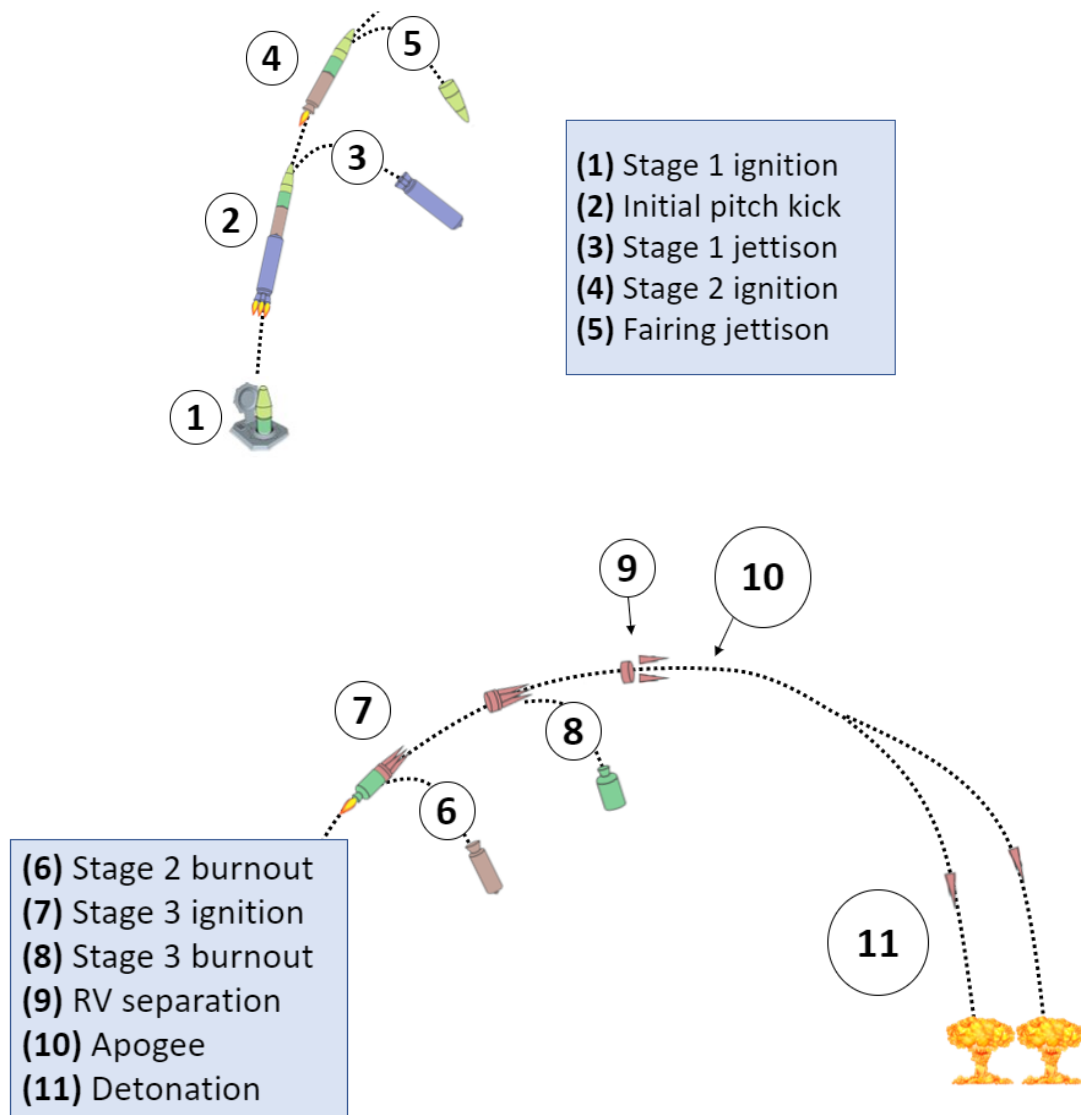


Figure 3.3: Architecture #1 ConOps

Architecture 2 includes the hypersonic glide vehicle, which introduces some extra complexities into the ConOps. The vehicle initially conforms to the standard ICBM launching procedure, with sequential staging. Instead of a post boost vehicle, however, the glider is deployed. The glider acts like a rock “skipping” in and out of the atmosphere as it closes the distance to the target. Note that this behavior adds to its survivability, making it harder to intercept. This is summarized below in Figure 3.4.

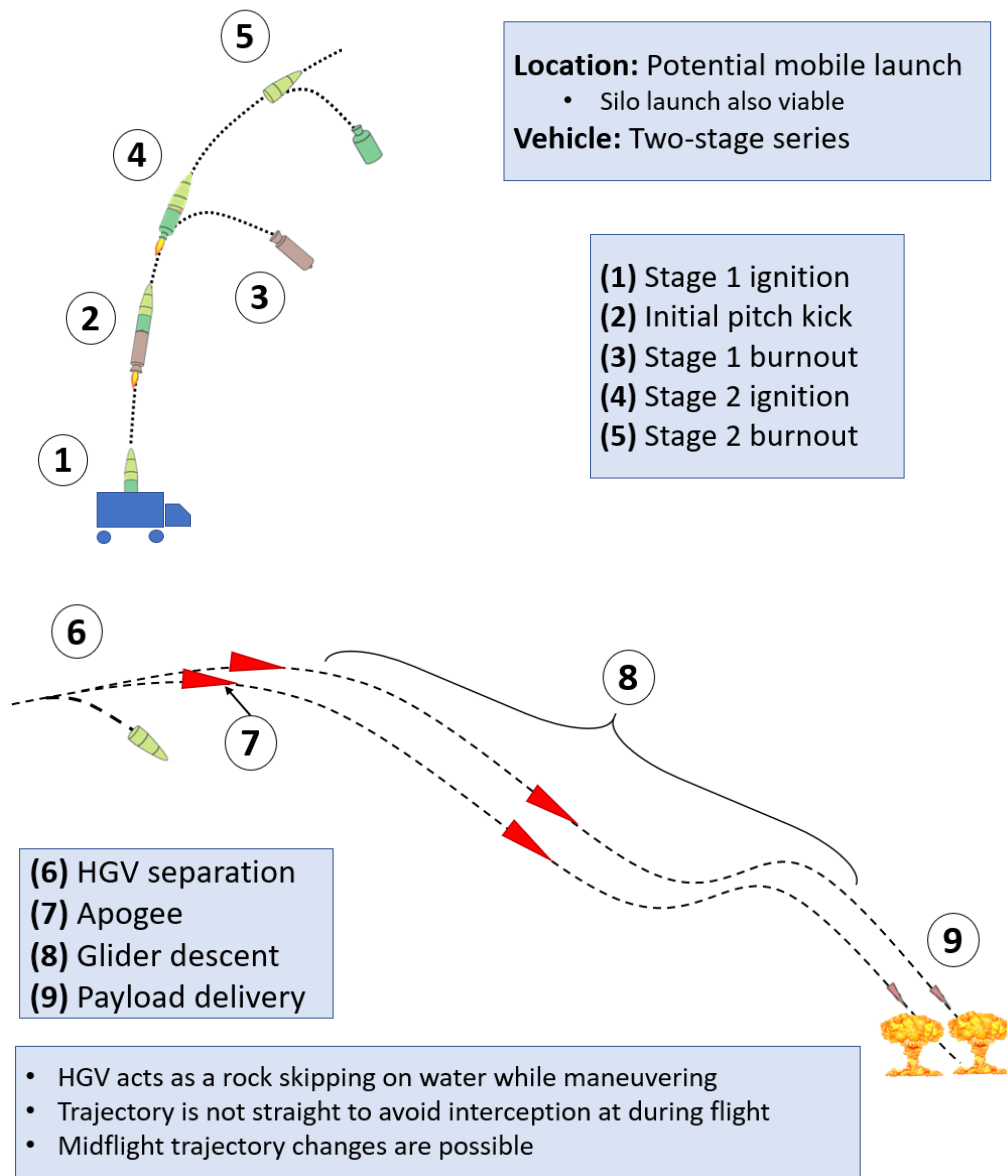


Figure 3.4: Architecture #2 ConOps

3.3 Selected Architecture

System architecture #1, the conventional ballistic missile, was the selected architecture. As the customer’s mission is directly tied to national security, risk was an important factor in the down-selection process. The first system architecture has low risk and proven technology that can operate out of the Minuteman III silos with more range than the original Minuteman III. Furthermore, this

system architecture does not require excessive redesigning as it will use the conventional reentry vehicle for the warheads and not the hypersonic glide vehicle. The second architecture requires immense design work for the hypersonic glide vehicle and the controlled hypersonic flight needs some maturity before it can be relied upon for national security missions. The drawbacks of this design are that it is not necessarily the most innovative design. This system had many technical constraints imposed by the dimensions of the silo and the customer requirements.

The following sections of this proposal will focus on the design decisions and results of the first architecture. It is important to note that while system architecture #1 was the chosen architecture, the analysis of the hypersonic glide vehicle continued. The goal is to eventually make the hypersonic glide vehicle compatible with the payload fairing for the chosen architecture as it was originally designed to be utilized on a different two-stage ICBM.

4 Vehicle Design and Sizing

Nomenclature

Symbols

A	=	Area
c_{del}	=	Characteristic velocity
C_D	=	Drag coefficient
D	=	Drag
D_{exit}	=	Exit diameter
D_{throat}	=	Throat diameter
g	=	acceleration due to gravity
L^*	=	Characteristic length
m_0	=	Initial mass
m_f	=	Final mass
m_s	=	Structural mass
m_p	=	Propellant mass
m_{PL}	=	Payload mass
\dot{m}	=	Mass flowrate
P_c	=	Chamber pressure
P_∞	=	Atmospheric pressure
T	=	Thrust
v	=	Velocity
ΔV	=	Change in velocity

Greek Letters

γ	=	Flight path angle
ε	=	Expansion ratio
η	=	Efficiency
μ	=	Standard gravitational parameter
ρ	=	Density of air
σ	=	Structural mass fraction
φ	=	Flight path angle
ψ	=	Ground range angle

Vehicle design modeling began first with fuel estimations based on necessary ΔV for the mission.

Next, trade studies for propellant selection and family sizing were completed for both architectures; with the optimal sizing selected, the tank sizing laid the base for the rest of the inboard profile. The inboard profile was then iterated until a positive design margin, and reasonable center of gravity was achieved.

4.1 ΔV Estimation

ΔV was determined using the USAF academy [6] estimate for burnout velocity, shown below in equation 4.1 and Figure 4.1 below. Accompanying the burnout velocity, additional estimates for drag and gravity loss were assessed as well to estimate a total ΔV . These losses were based on values taken from the *Elements of Space Launch Vehicle Design* textbook [7].

$$v_{bo}^2 = \frac{2\mu}{r_{bo}} \left(\frac{\sin \frac{\psi}{2}}{1 + \sin \frac{\psi}{2}} \right) \quad (4.1)$$

$$\Delta v_{loss} = -\frac{D}{m} - g \cdot \sin(\gamma) \quad (4.2)$$

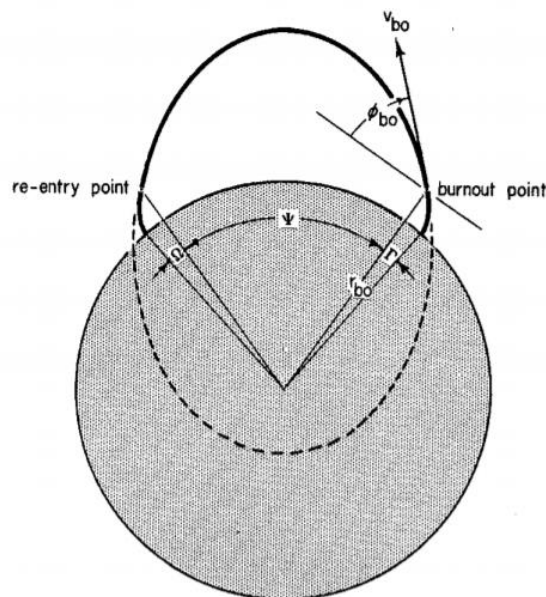


Figure 4.1: Ballistic trajectory geometry

Two different estimates were found based on both architectures; architecture 1 was estimated to need 30,512 ft/s, architecture 2 was estimated to need 26,247 ft/s. Values for drag and gravity loss were refined and iterated as the trajectory was defined. Architecture 2 was estimated much lower based on glide capability; this number is less certain due to the trajectory being much less refined as more research is needed into the hypersonic flight portion as will be discussed later.

4.2 Propellant Selection

Storable liquid and solid propellants were considered for both architectures based on the 20-year lifecycle requirement. The key parameter driving propellant trade studies was the I_{sp} values. The solid propellants considered were based on commercial motors found in the Northrop Grumman catalog. Values for liquid propellants were obtained from astronautix.com or calculated based on the stoichiometric mixture ratio in NASA’s Chemical Equilibrium with Applications (CEA). Table 4.1 below shows a full list of the considered propellants.

Table 4.1: Specific impulses of possible propellants

Propellant	I_{sp} (s) Seal Level	I_{sp} (s) Vacuum
JP-10/H₂O₂	290	330
Kerosene/N₂O	260	281
Ethanol/H₂O₂	268	292
Kerosene/N₂O₄	276	301
N₂O₄/MMH	288	313
Ethanol/N₂O	255	276
LCS1 (Solid)	279	-
Castor 120 (Solid)	280	-
Orion 50S XLG (Solid)	272	-
AP/PBAN/Al (Solid)	285	-

A main concern in selection was the corrosiveness and toxicity of hydrogen peroxide and nitrogen tetroxide. Additional extensive research was done to assess whether hydrogen peroxide would be suitable for the 20-year lifecycle requirement. Due to lack of time and resources the same assessment was not done for nitrogen tetroxide, making this one of the weakest points in the design of architecture 1.

Hydrogen peroxide is dense, storable, non-cryogenic, and has monopropellant capabilities; however, it is considered by many to be a poor choice of an oxidizer. A key concern about hydrogen peroxide is its handling complexities and to some, its storability as an alcohol-based propellant. To address these concerns, a leading expert on hydrogen peroxide, Mark Ventura of

Ventura Energy Systems LLC, was consulted. Mr. Ventura spoke about the storability of hydrogen peroxide in his past published work and experiments on the topic. Hydrogen peroxide decomposes at differing rates depending on its temperature, and throughout the years several experiments have been conducted studying this loss ratio. In Figure 4.2, a compilation of studies looking at peroxide decomposition at varying temperatures shows a trend that newer studies estimate peroxide decomposition being incredibly minor this figure comes from Mark Ventura’s paper *Rocket Grade Hydrogen Peroxide (RGHP) for use in Propulsion and Power Devices - Historical Discussion of Hazards* [8].

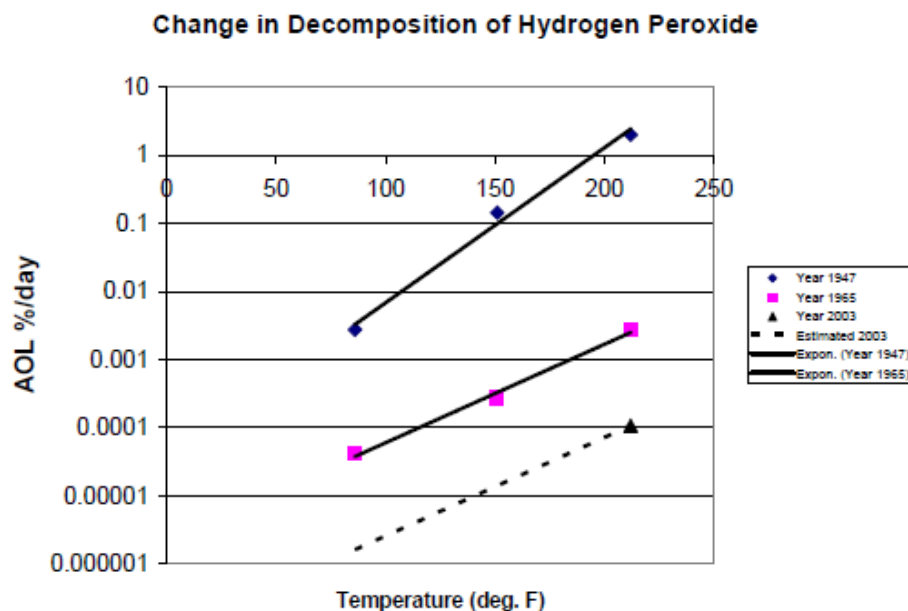


Figure 4.2: Decomposition of Hydrogen Peroxide

Estimated losses in 2003 show that if kept at 100 degrees Fahrenheit, a temperature an underground silo in the mid-west will surely be kept below, an expected alcohol loss per day is nearing 0.000001%. Using this loss rate after 20 years 98% hydrogen peroxide will be diluted to 97.27%, with a minimal resulting drop in I_{sp} . In the professional setting Stripe Aerospace will consult with Mark Ventura for lessons on handling the propellant grade, [9] which is comparable in complexity to other high-performance oxidizers such as liquid oxygen or nitrogen tetroxide.

The storability of JP-10 as a propellant is also questionable, but an AFRL Propulsion Directorate fuels service life study indicates that the propellant shelf-life will be extended from 19 to 28 years [9]. This makes JP-10 a viable propellant for silo storability in the context of this design.

4.3 Launch Vehicle Family Sizing Analysis

The family sizing trade study was used to determine what percentage of the total ΔV would be carried in each stage. This was done using simple computation in excel, using the rocket equation and relationships from the structural factor (σ), with an estimated structural mass fraction and mixture ratio. Using the rocket equation, and relationships from the mass and structural ratio, the family sizing spreadsheet created mass breakdowns of structural, propellant, and total stage mass. In the case of liquid propellants, an initial value of 0.07 was used and this number was iterated and changed as the inboard profile evolved. Structural mass fractions were provided in the NGC catalog for each commercial solid propellant. Estimations for mixture ratios were based on previous vehicles engine designs with the same propellants, as provided by Astronautix.com. The final selection was based on what combination provided the lowest gross lift-off mass. The equations used are listed below:

$$\Delta V = g_0 I_{sp} \ln \left(\frac{m_0}{m_f} \right) \quad (4.3)$$

$$\sigma = \frac{m_s}{m_s + m_p} = \frac{m_s}{m_0 - m_{PL}} \quad (4.4)$$

From the ΔV analysis, the following propellants were selected: AP/PBAN/Al solid (stage 1), MMH/N₂O₄ (stage 2), JP10/98% H₂O₂ (stage 3). These propellants were ultimately selected based on their efficiency, as they resulted in the lowest gross liftoff masses throughout the trade

study. Additionally, it was decided to design a custom solid motor for stage 1 to avoid resizing of a commercial engine.

Architecture 1 ΔV was split into the following: 20% ΔV first stage, 35% ΔV second stage, 45% ΔV third stage. Architecture 2 ΔV was split in the following: 58% ΔV first stage, 42% ΔV second stage. A full mass breakdown of all stages for architectures 1 is shown below in Table 4.2:

Table 4.2 Mass Breakdown of Selected Architecture

Architecture 1				
Δv_{total}	30511.8			ft/s
	stage 1	stage 2	Stage 3	
ΔV ratio	20%	35%	45%	
Isp	285	300.5	296.7	
MR	1	1.65	7	
Diameter	86.6	70.9	59.1	in
M_s	2833.8	1392.0	727.5	lb _m
M_p	37648.6	21807.9	8894.5	lb _m
M_0	40482.4	23199.9	9462.5	lb _m
GLOM	74142.6			lb _m

4.4 Inboard Profile Design Process

The following processes were done for both architecture 1 and 2; architecture 1 being the conventional three-stage ballistic missile (modeled after Minuteman III), and architecture 2 being a much more innovative but high-risk design with two ballistic stages followed by a hypersonic glide vehicle. During downsizing, architecture 1 was selected to be the final architecture, so the inboard profile results will primarily be discussing architecture 1.

4.4.1 Tank Design

The process of designing the inboard profile began first with tank sizing, based on the propellant density and ΔV requirements per stage. Liquid propellant tanks were estimated to be cylindrical with elliptical domes and the solid motor casing was assumed to be a cylinder. In both cases, the

tank/motor casing walls doubled as the body of the rocket. If either the fuel or oxidizer did not need the full capacity of the rocket diameter, the tank was modeled as a sphere held in place by struts. In addition to the required propellant, residual, ullage, and start-up propellant was also accounted for using mass estimation relationships. Residual propellant was estimated to be 2% of required propellant. Start-up transients were estimated to take 1 second and the required propellant for it was modeled as $m_{start-up} = t_{start-up} \times \dot{m}$. Additional volume was also added the tank sizing of liquid propellants to account for ullage (additional 3%) and tank shrinkage (additional 2%). In the design of the solid motor casing, a volume was added for the propellant grain thrust tailoring consumption (additional 10%), and to account for insulation to protect the casing and ignition system (additional 2%). Tank sizing dimensioning can be seen in Figure 4.3.

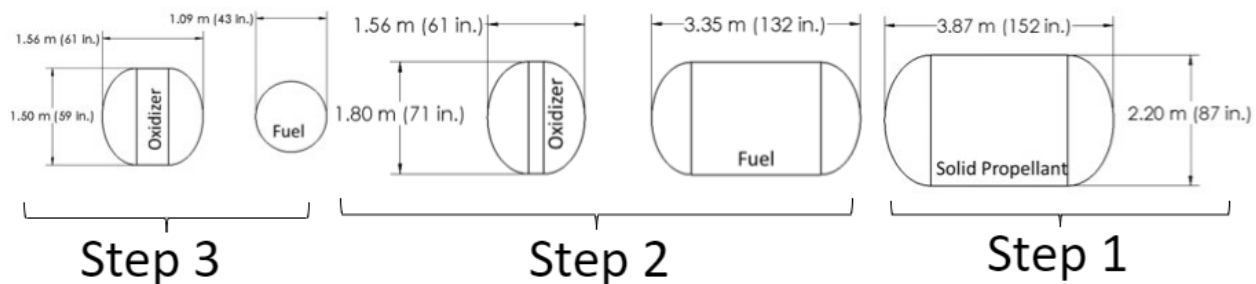


Figure 4.3: Final Tank Dimensions for Architecture 1

4.4.2 Solid Motor/Liquid Engine Sizing

The engine dimensioning was done so as a function of thrust, chamber pressure, throat area, and specific impulse. The required thrust was found by selecting a desired T/W ratio and the gross lift off mass found using the family sizing calculations. A T/W ratio of 2.5 was selected for all stages of both architectures. Specific impulse was pre-determined based on selected propellant combination. Using chamber pressure and throat area as inputs, based on existing engines, the following outputs can be calculated as follows:

$$A_{throat} = \frac{c_{del} T_{vac}}{P_c g_0 I_{sp-vac}} \quad (4.5)$$

$$T_{vac} = \frac{T_{SL}}{1 - \frac{P_\infty c_{del} \epsilon_{nozzle}}{P_c g_0 I_{sp-vac-del}}} \quad (4.6)$$

Using T_{vac} as a reference, the inputs of chamber pressure and throat area were iterated until T_{vac} was desirable. The criteria for the first stage is that T_{vac} must be large enough that $T_{SL} \geq T_{required}$, this can be verified using the following relationship:

$$T_{SL} = T_{vac} - P_\infty A_e \quad (4.7)$$

It can be assumed that the upper stages will be performing in a vacuum environment so the criteria for upper stages is simply $T_{vac} \sim T_{required}$. The sizing for the nozzle length, chamber diameter and chamber length, and convergent section length were calculated u% of ideal sing the following estimations: Assuming the nozzle is 80% length of ideal 15° half angle cone, the nozzle length is,

$$L_{nozzle} = \frac{(D_{exit} - D_{throat})(\%length)}{2 \tan 15} \quad (4.8)$$

Values for L^* are obtained from [10] based on propellant choices and 0.9 is used for

$L_{thRatio_{chamber}}$. The combustion chamber length is found as,

$$L_{comb\ chamber} = \left(\frac{4(L^*)(A_{throat})(L_{thRatio_{chamber}})}{\pi} \right)^{\frac{1}{3}} \quad (4.9)$$

Finally, the convergent section length is calculated by

$$L_{conv} = \frac{D_{chamber} - D_{throat}}{2 \tan(\alpha_{conv\ section})} \quad (4.10)$$

Where α convergent section angle (30° used in calculation).

A table listing key parameters for motor/engine dimensioning and performance will be shown below in Table 4.3. Following the table will be nozzle geometry for each of the three stages in Figure 4.4, Figure 4.5, and Figure 4.6.

Table 4.3: Summary of Motor/Engine Parameters

Parameter	Stage 1	Stage 2	Stage 3
T/W	2.5	2.5	2.5
Thrust (lbf)	174,452	94,355	28,075
I_{sp} (s)	285	303.89	327.11
Length (ft)	6.69	7.77	5.41
Expansion Ratio	12.6	57	102
Exit Velocity (ft/s)	9,186	5,479	9,543

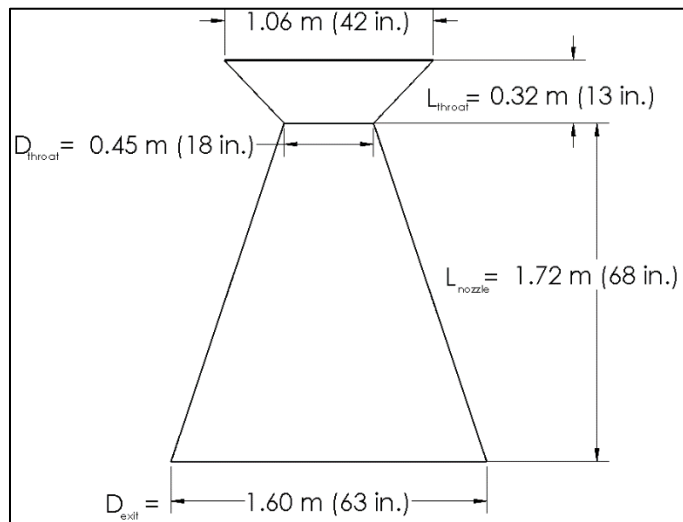


Figure 4.4: Stage 1 Nozzle Geometry

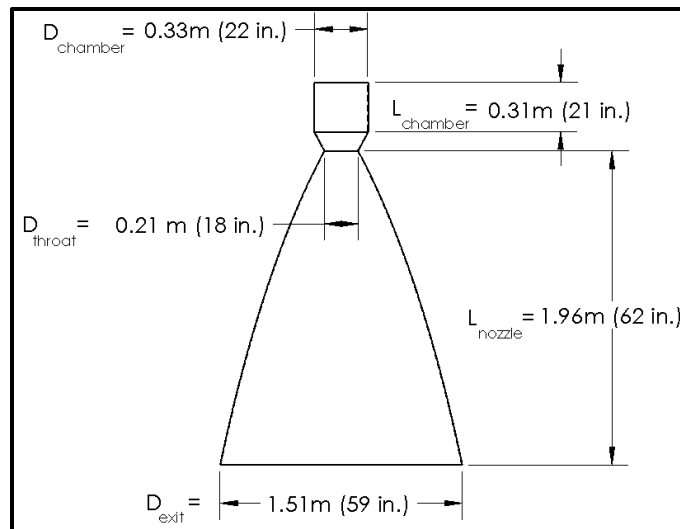


Figure 4.5: Stage 2 Engine Geometry

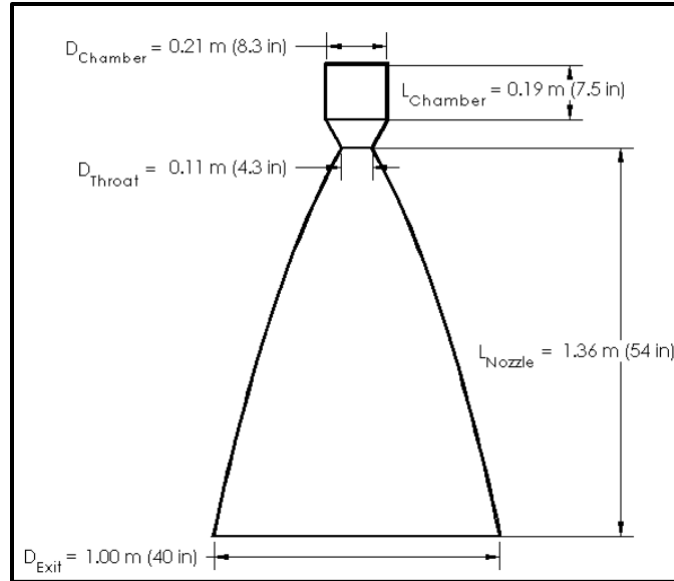


Figure 4.6: Stage 3 Engine Geometry

4.4.3 Pump Sizing

Each liquid propellant requires a pump to push it into the engine combustion chamber at the correct pressure and mass flow. To estimate what pumps are needed, a calculation provided by Humble [11] will provide the power required. The equation is as follows:

$$p_{req} = \frac{g_0 \dot{m} H_p}{\eta_p} \quad (4.11)$$

The pump head rise is defined as:

$$H_p = \frac{\Delta p_p}{g_0 \rho} \quad (4.12)$$

For Δp_p , the assumption of an unpressurized tank was used as a method for compensating against pressure drop. Therefore, the value used for each pump was the pressure inside the combustion chamber with an additional 20% added to account for the injector pressure drop [10]. The results of this process are summarized in the Figure 4.7 below.

Stage 2 Pumps		Pump Head (ft)	Mass Flow (lb _m /s)	Horse Power
Oxidizer	N2O4	2090	167.3	795.1
Fuel	MMH	3422	101.4	788.5
Stage 3 Pumps		Pump Head (ft)	Mass Flow (lb _m /s)	Horse Power
Oxidizer	H2O2	4150	79.6	751.9
Fuel	JP10	6401	11.5	165.7

Figure 4.7: Architecture 1 Pump Requirements

These horsepower requirements would be used in future pump selection.

4.4.4 Post-Boost Vehicle

A post-boost vehicle (PBV) was required to help reach the desired re-entry release window as well as to orient itself as it reaches the appropriate release window. It was designed to fit 2 re-entry vehicles as requested by the RFP and will hold an avionics bay which will house all electronics and the missile guidance system. To help reach our desired release window the PBV will have a primary gimbaled booster engine capable of 315 lb_f of thrust to allow the payload to be on course by making any velocity corrections. The PBV will also contain 8 attitude control thrusters to properly orient the PBV and have an optimal re-entry vehicle release. A clear image of the PBV design can be seen in Figure 4.8 below.



Figure 4.8: Post-Boost Vehicle Design

4.4.5 Fairing

To ensure the payload successfully reaches its target, a fairing will be used to enclose and protect the re-entry vehicles during the ascent phase of the mission. It will be elliptically shaped with a typical clam shell release design and a blunt nose for distributed heating. With a length of 11.17ft and a base of 4.9ft the fairing is big enough to encapsulate the avionics bay and both re-entry vehicles with extra room to spare. The fairing will be manufactured out of sandwich material composed of composite material and an aluminum honeycomb core filled with cork for preventative heating during ascent. Figure 4.9 gives an image of the fairing design used for the ICBM.



Figure 4.9: Clam shell release fairing design

4.4.6 Re-entry Vehicle

In order to protect the warheads from heating during re-entry, a re-entry vehicle (RV) was designed to take all the thermal heating during atmospheric descent. Both the nuclear warhead and arming mechanism will be a combined 80 in. in length and conically tapered with a 22 in. base as requested by the RFP and with the RV design encapsulating the warhead, the total length becomes 96.4 in. with a 23.6 in. base. A main feature of the re-entry vehicle is a spin stabilizing mechanism to allow for more precision during the descent phase. The nose tip and body of the RV will be composed of carbon-carbon material which allows to take all thermal heating during its re-entry phase protecting the warhead and tracking electronics. Figure 4.10 provides a dimensioned CAD drawing of the RV.

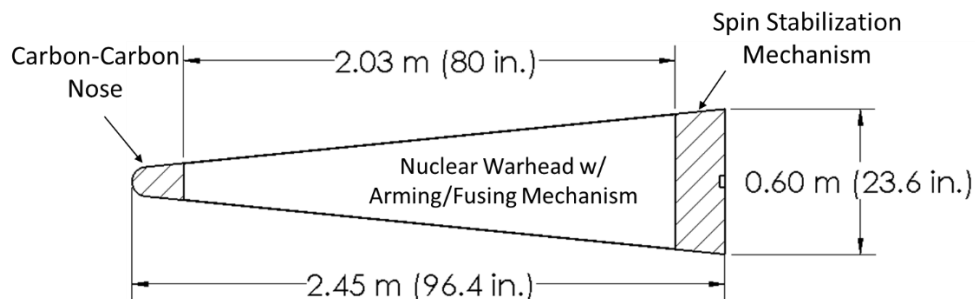


Figure 4.10: RV design and dimensions

4.4.7 Separation Devices

The separation devices chose are all devices that have been previously used and are known to be reliable, as provided in a trade study from NASA [12]. The first stage solid motor jettison uses thrust reversal to separate; when using thrust reversal, the main concern is chugging, to avoid this, nominal coast time has been allocated to avoid any damage to remaining stages. The second and third stage jettison, both of which are liquid engines, use a v-clamp; with explosive bolts. Redundancy will be accounted for (two rings of 8 bolts) to ensure a clean and debris-free separation. The fairing separation, occurring at 315,000 ft will be using 3 helical compression springs; additionally, the fairing will be a typical clamshell release for simplicity. Finally, the reentry vehicle/payload release will also use helical compression springs. In the event that the conventional reentry vehicle is used 5 springs will be implemented, in the event the hypersonic glide vehicle used, 10 springs will be implemented. In both cases, tip off rates of 0.5 deg/sec or less are ensured. The compression springs used will be commercial helical compression springs.

4.4.8 Scale Drawing and Mass Properties

The rest of the inboard profile such as intertanks, interstages, space accommodation for engine equipment and upper stage attachment, as well as thrust and ground attach structures were estimated using basic relationships shown in Table 4.4 below.

Table 4.4: Intertanks, Interstages, and extra accommodation dimensioning

Intertanks	Leave D/4 separation between fuel and oxidizer tank
Interstages	Leave engine length to accommodate the engine between stages
Space accommodation	Leave D/8 space for engine equipment and upper stage attachment

Following the sizing of the vehicle components, a scale drawing was produced in SolidWorks. The

scale drawing is shown below in Figure 4.11, with a mass breakdown in Figure 4.12.

With the rocket modelled, the mass properties were assessed next. The center of mass was calculated using SolidWorks, and the center of pressure was calculated using the Rogers Modified Barrowman method based on external geometry. Additionally, the moments of inertia for pitch and roll were calculated in SolidWorks. These values are shown below in Table 4.5.

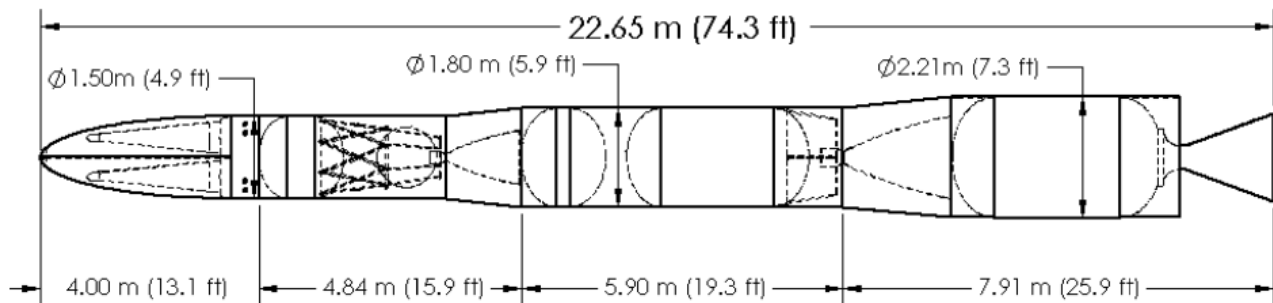


Figure 4.11: Scale Drawing of Vehicle

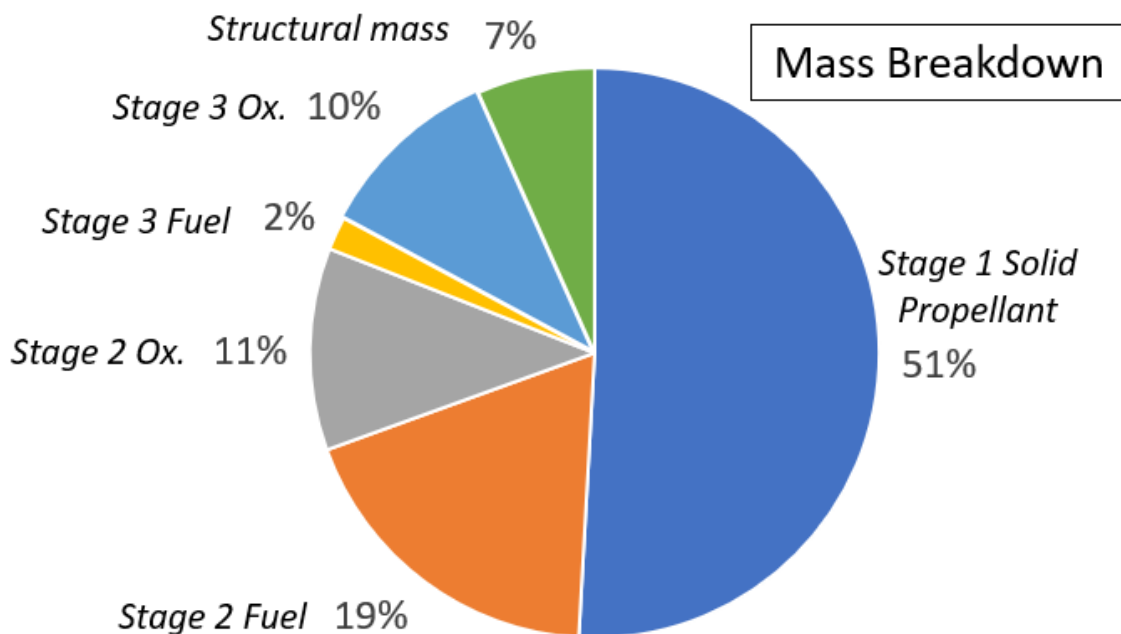


Figure 4.12: Mass Breakdown of Vehicle

Table 4.5: Mass Properties of Vehicle.

CM	28	ft
CP	9.9	ft
J_{Pitch}	38,851	lb_m-ft²
J_{roll}	3,924	lb_m-ft²

Figure 4.13 provides a view of the center of mass and center of pressure on the scale drawing.

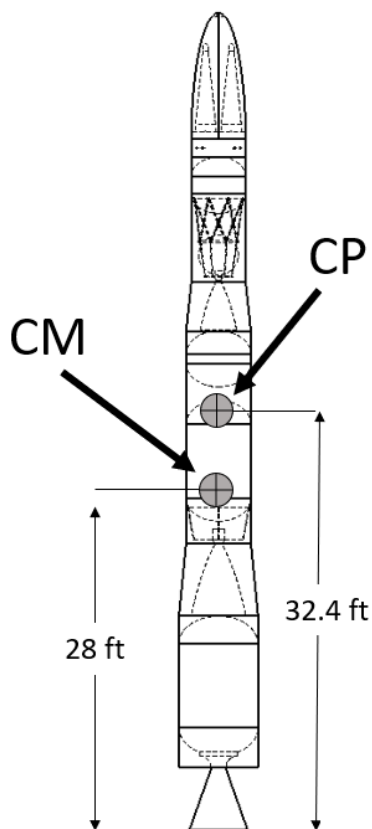


Figure 4.13: Diagram with CM and CP

4.4.9 CAD Model Views

Below in Figure 4.14 is CAD model of the selected architecture displayed in a 2-view image and Figure 4.15 is an image displaying the final configuration of the ICBM.

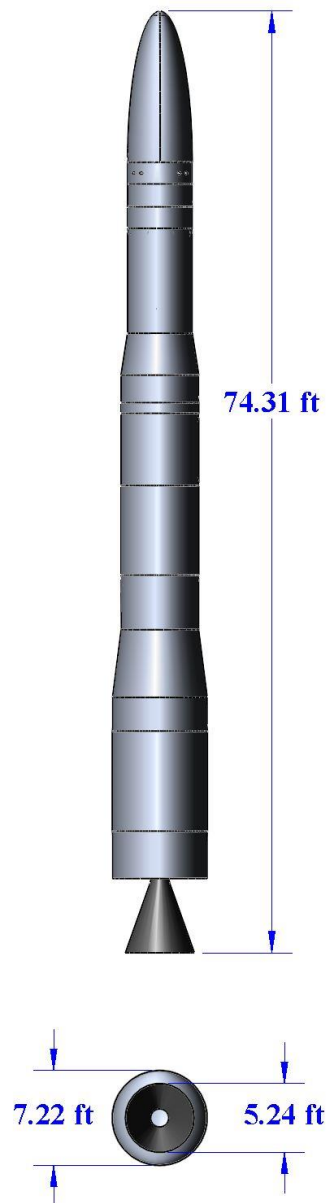


Figure 4.14: Side and bottom view of ICBM

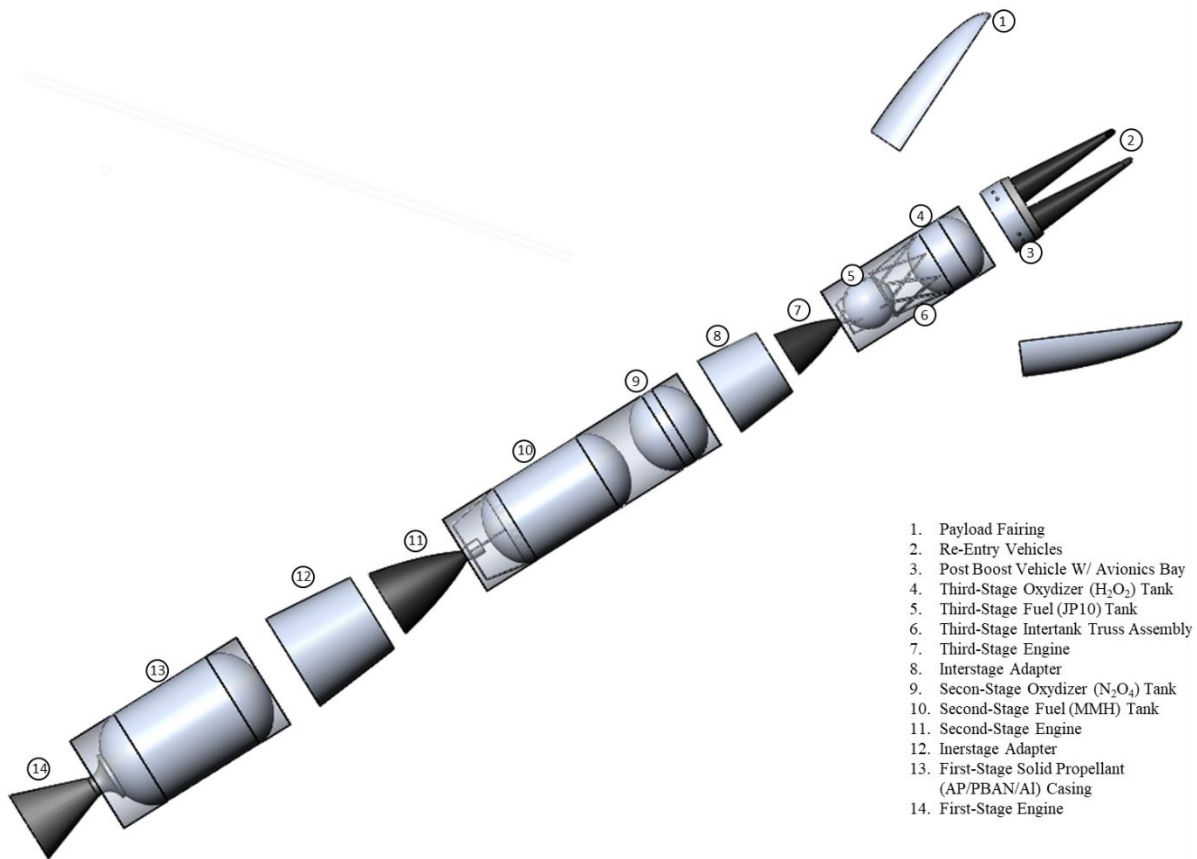


Figure 4.15: ICBM configuration

5 Trajectory

Nomenclature

Symbols

C_D	=	Drag coefficient
d	=	Great-circle distance
D	=	Drag
g	=	acceleration due to gravity
h	=	Altitude
L	=	Lift
L/D	=	Lift to drag ratio
m	=	Mass
\dot{m}	=	Mass flowrate
q	=	Dynamic pressure
q_w	=	Heat flux
r	=	Radial distance from center of earth
t	=	Time
T	=	Thrust
T_w	=	Wall temperature
x	=	Total distance
v	=	Velocity

Greek Letters

β	=	Azimuth angle
γ	=	Flight path angle
λ	=	Latitude
Λ	=	Longitude
ρ	=	density of air
σ	=	Bank angle or Standard deviation
ω_E	=	Rotational speed of Earth
ϕ	=	Gimbal angle
ψ	=	Gimbal angle

In order to validate that the design meets the range and payload deployment requirements specified by the RFP, a trajectory analysis must be compiled. A profile of the boost, coast, and reentry of the vehicle may be modelled in an optimization process. By optimizing the trajectory, the vehicle may be designed to meet the RFP requirements in the most efficient way possible.

5.1 Ballistic Trajectory Approach and Modelling

Upon completion of the ICBM sizing and inboard profiles, the mass (propellant and structure) data and engine performance parameters were tabulated to be integrated into the trajectory analysis. Several equations of motion from Holt Ashley's text were used to model the motion of the rocket during boost and coast [13]. These 3-DOF equations of motion are shown below in equations 5.1 through 5.8.

$$m(t) = m_0 - \dot{m}t \quad (5.1)$$

$$\frac{dv}{dt} = \omega_E^2 r \cos \lambda [\sin \gamma \cos \lambda - \cos \gamma \sin \beta \sin \lambda] - g \sin \gamma + \frac{T \cos \varphi \cos \psi}{m} - \frac{D}{m} \quad (5.2)$$

$$\frac{d\gamma}{dt} = \frac{v \cos \gamma}{r} + 2\omega_E \cos \beta \cos \lambda + \frac{\omega_E^2 r \cos \lambda}{v} (\cos \gamma \cos \lambda + \sin \gamma \sin \beta \sin \lambda) - \frac{g \sin \gamma}{v} + \frac{T \sin \varphi}{m} \quad (5.3)$$

$$\frac{d\beta}{dt} = -\frac{v \cos \gamma}{r} \cos \beta \tan \lambda - 2\omega_E (\sin \lambda - \tan \gamma \sin \beta \cos \lambda) - \frac{\omega_E^2 r \cos \beta \sin \lambda \cos \lambda}{v \cos \gamma} + \frac{T \cos \varphi \sin \psi}{mv \cos \gamma} \quad (5.4)$$

$$\frac{dh}{dt} = v \sin(\gamma) \quad (5.5)$$

$$\frac{d\Lambda}{dt} = \frac{v \cos \gamma \cos \beta}{r \cos \gamma} \quad (5.6)$$

$$\frac{d\lambda}{dt} = \frac{v \cos \gamma \sin \beta}{r} \quad (5.7)$$

$$D = C_D S_{ref} \frac{1}{2} \rho v^2 \quad (5.8)$$

These equations of motion consider the curvature and rotation of a spherical Earth and utilize a tangent-trajectory coordinate system shown below in Figure 5.1. Something to note is in this coordinate system is that an azimuth angle of zero degrees is defined as due east, 90 degrees as due north, and so on. Note that for reentry analysis, the equations must be modified slightly. This analysis is performed in section 5.2.2. Additionally, the range is calculated using the haversine formula shown as follows:

$$d = 2r \sin^{-1} \left(\sqrt{\sin^2 \left(\frac{\lambda_2 - \lambda_1}{2} \right) + \cos \lambda_1 \cos \lambda_2 \sin^2 \left(\frac{\Lambda_2 - \Lambda_1}{2} \right)} \right) \quad (5.9)$$

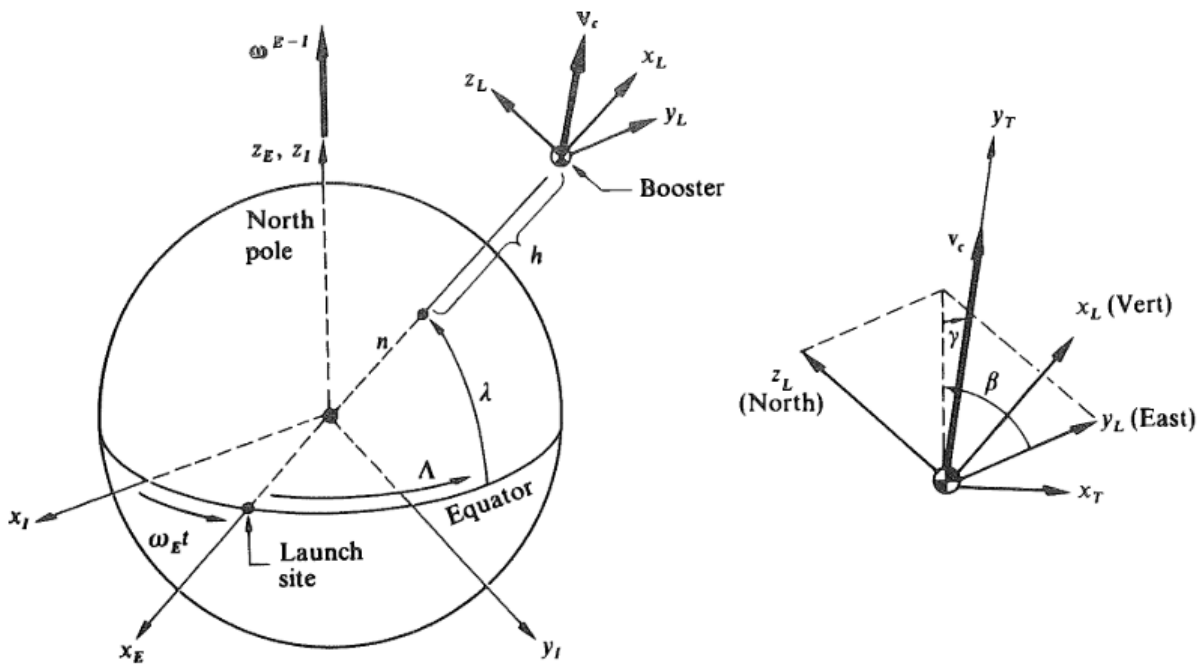


Figure 5.1: Graphical representation of Coordinate System for Equations of Motion [13]

A key assumption made for the trajectory analysis is that the vehicle's thrust changes with altitude due to pressure differences and maintains a constant I_{sp} . Additionally, staging events were also assumed to be instantaneous with a one second delay before igniting the next stage's engine. The US 1976 standard atmosphere model was integrated into the code to simulate changes in air properties with altitude [14], and the Titan II drag model (see Figure 5.2) was used to represent a dynamic drag coefficient. The effects of lift were ignored for the boost and coast portion of the trajectory. Thrust vectoring was also not modeled and eliminated any steering losses. Finally, the

post boost vehicle is not modelled to perform course corrections or provide extra velocity and is thus treated as inert mass during coast.

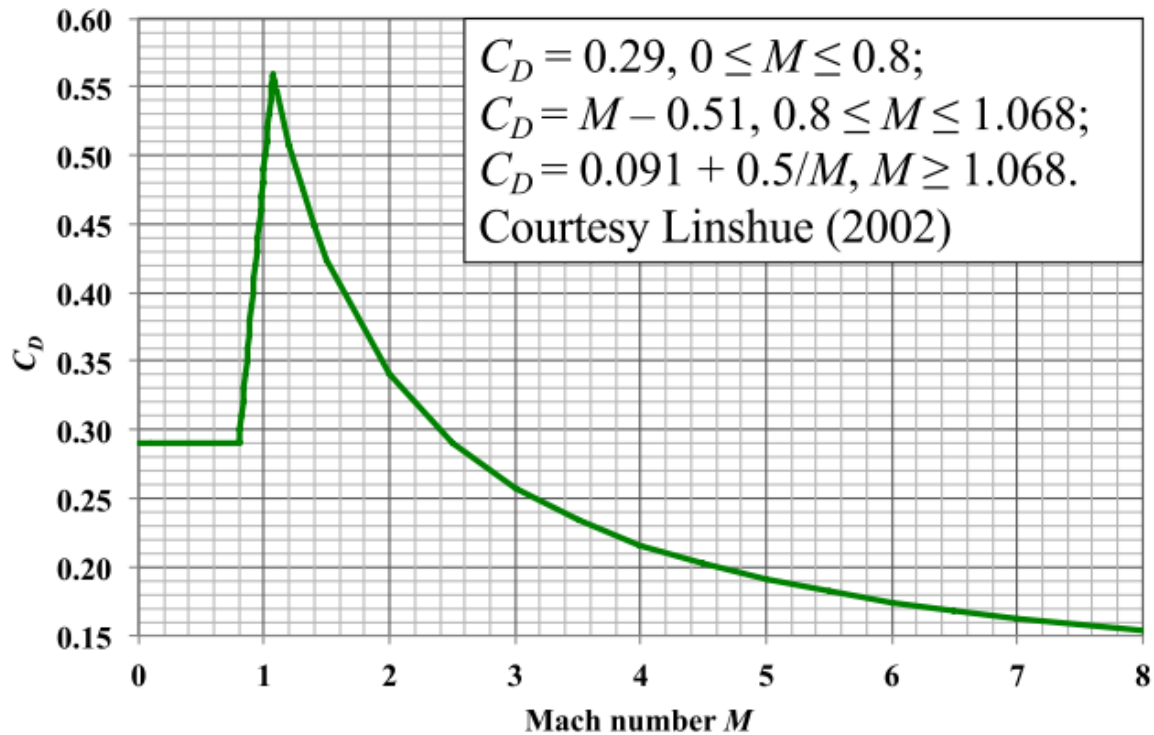


Figure 5.2: Titan II Drag Model (Provided by Faculty Advisor)

The equations of motion are implemented into MATLAB and the *ode45* function was used to numerically integrate them with a time step of 0.01 seconds. The execution of this code generated the necessary parameters required to define the flight profile of the ICBM every second from launch to reentry.

The code generated a table of all the flight parameters from which the maximum dynamic pressure (max q) flight conditions were extracted. This data was later used to assess the loads acting on the theoretical vehicle during max-q and design the appropriate structure (see Section 6). Systems Tool Kit (STK) developed by Analytical Graphics Inc. was utilized to optimize the trajectory generated by the equations of motion. By plugging the requirements into the program, a nominal trajectory would be generated with a dataset of required parameters such as velocity, pitch

angle, and altitude. In order to meet the requirements of this STK nominal trajectory with the MATLAB code, the pitch kick angle/time were varied randomly in a Monte-Carlo fashion until convergence was observed. **Figure 5.3** below demonstrates a basic overview of what the results of this procedure might look like. The red lines represent ascent trajectories that properly inject into the black STK trajectory.

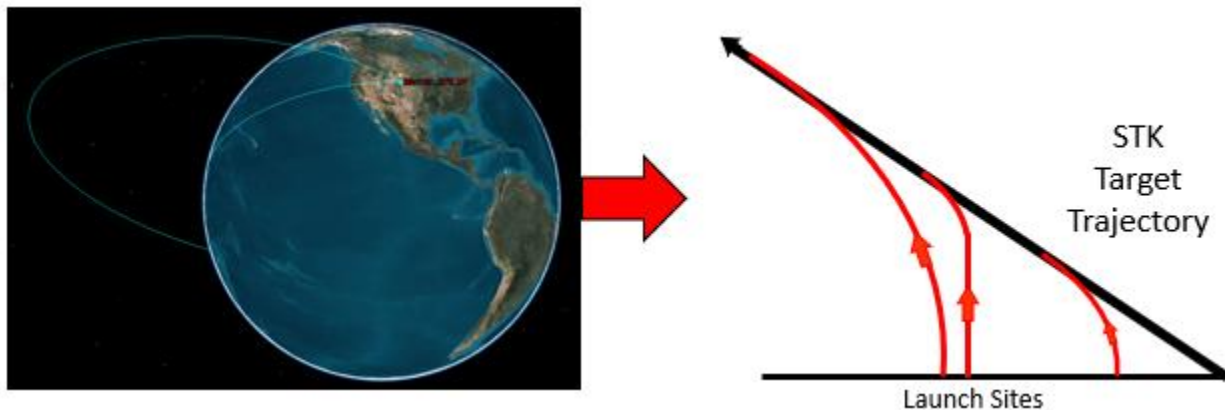


Figure 5.3: Overview of trajectory optimization

Following the Monte-Carlo analysis, the potential injection trajectories were trade-studied based on atmospheric losses, max-q loads, and time to injection.

The dynamic equations of atmospheric reentry are modeled in a separate MATLAB code once optimization is complete. The initial conditions of the reentry trajectory analysis code come from the optimized ballistic trajectory and is integrated into the ballistic trajectory code to create a launch-to-impact trajectory analysis tool. The reentry trajectory analysis code specifically takes the flight path angle and speed of the RV from the ballistic trajectory section at a specified release point altitude for the RVs.

5.2 Optimized Trajectory to Meet Requirements

To demonstrate that the vehicle can meet the key RFP requirements, an example scenario is laid out. In this mission scenario, the missile is launched from Warren AFB (41.15°N, 104.9°W) and

targets an arbitrary location in the Indian Ocean. Constraints for the range and flight time are inputted into STK to develop the nominal trajectory that the MATLAB code will converge towards. The final optimized trajectory is summarized in the following sections.

5.2.1 Ascent (Boost) Trajectory

The ascent trajectory is the portion of the trajectory that is optimized to match STK. The optimized values are shown in Table 5.1. Figure 5.4 shows the time history of the flight path angle, velocity, Mach number, dynamic pressure, altitude, and total distance as a function of time. An important note is that the total ΔV produced from this trajectory is somewhat less than the design ΔV used to size the vehicle. This means that resizing could be done for further optimization.

Table 5.1: Ascent Trajectory Analysis Results

Parameter	Value	Unit
Initial β	10	deg
t_{burnout}	241	s
$t_{\text{kick, gravity turn}}$	10	s
$\gamma_{\text{kick, gravity turn}}$	16	deg
$\gamma_{\text{kick, stage 2}}$	5	deg
$\gamma_{\text{kick, stage 3}}$	3	deg
h_{burnout}	107.5	kft
V_{burnout}	25.1	kft/s
$V_{\text{gravity loss}}$	-4.15	kft/s
$V_{\text{drag loss}}$	-0.55	kft/s
ΔV_{total}	29.8	kft/s

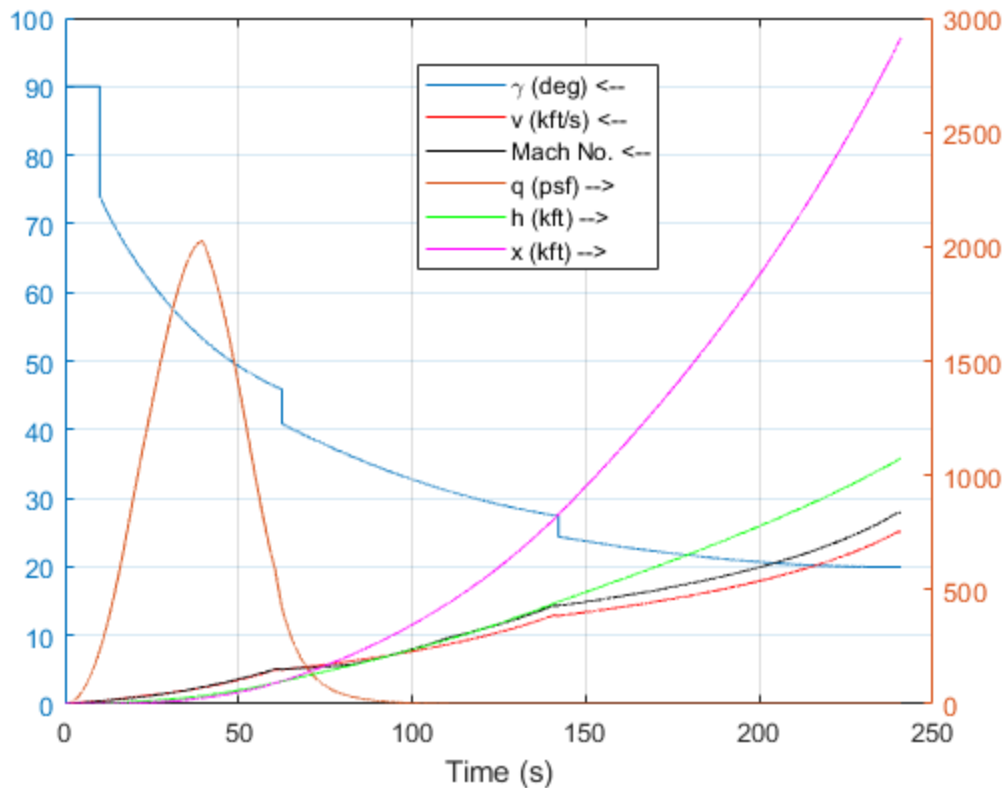


Figure 5.4: Ascent Trajectory Parameters vs. Time

Figure 5.5 shows weight and mass flow rate vs time while and Figure 5.6 shows thrust and drag vs time. These plots show the effects of staging on the vehicle.

After the boost phase of the trajectory, thrust is terminated and excess structure is detached from the vehicle. The missile begins the coast phase which is the majority of the flight and results for the coast are shown in section 5.2.3. The coast phase ends at the specified release altitude and the parameters at that point define the initial conditions for the reentry.

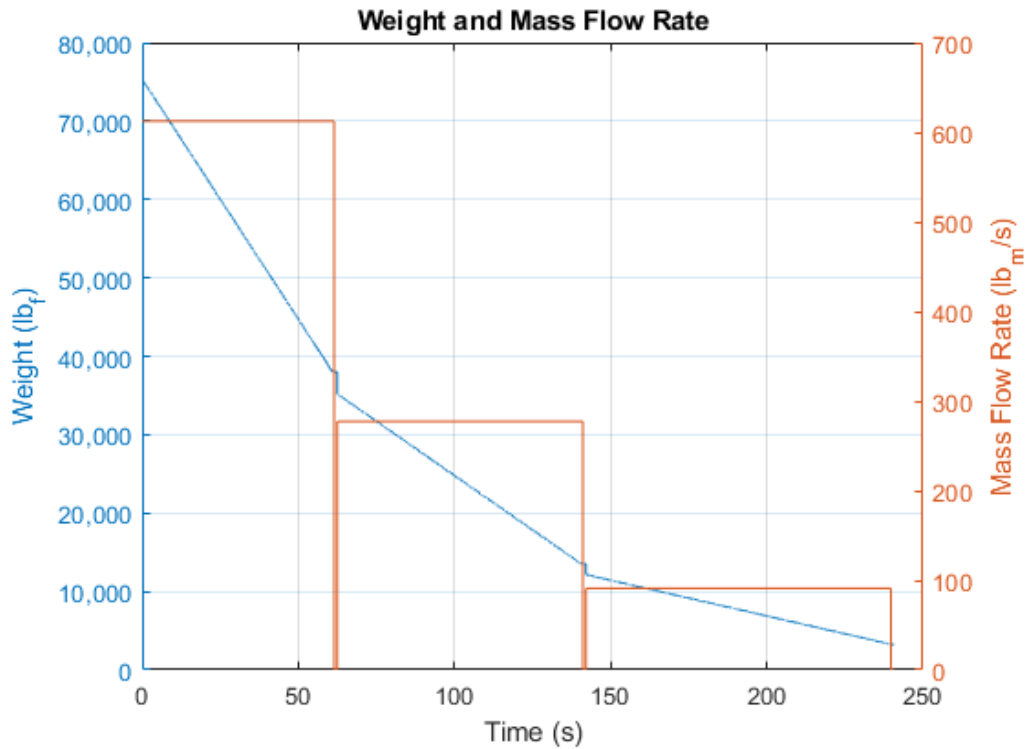


Figure 5.5: Time history of vehicle weight and propellant mass flow rate during boost

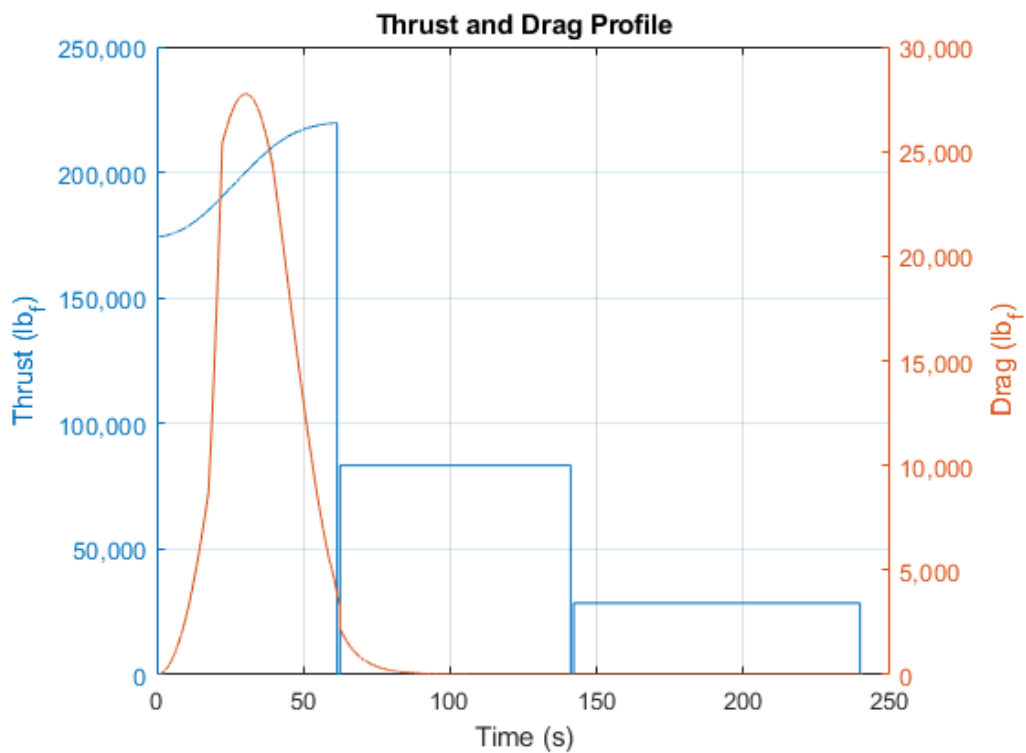


Figure 5.6: Time history of thrust and drag during boost ascent trajectory

5.2.2 Reentry Trajectory

Modeling the trajectory of the reentry vehicle (RV) is similar to what was done previously. Slight adjustments need to be made to pitch and azimuth rate equations to account for lift [15].

Additionally, any thrust component was removed entirely since the RVs do not produce thrust.

$$\frac{d\gamma}{dt} = \frac{v \cos \gamma}{r} + 2\omega_E \cos \beta \cos \lambda + \frac{\omega_E^2 r \cos \lambda}{v} (\cos \gamma \cos \lambda + \sin \gamma \sin \beta \sin \lambda) - \frac{g \sin \gamma}{v} + \frac{L \sin \sigma}{mv} \quad (5.10)$$

$$\frac{d\beta}{dt} = -\frac{v \cos \gamma}{r} \cos \beta \tan \lambda - 2\omega_E (\sin \lambda - \tan \gamma \sin \beta \cos \lambda) - \frac{\omega_E^2 r \cos \beta \sin \lambda \cos \lambda}{v \cos \gamma} + \frac{L \sin \sigma}{mv \cos \gamma} \quad (5.11)$$

The reentry analysis made the assumptions of constant mass, constant drag coefficient and constant lift to drag ratio. The following values were assumed: $C_D = 0.35$, $L/D = 0.1$, $m = 1,500$ lb_m. The C_D and L/D values are based on data provided by [16] for a sphere cone at zero angle of attack. Table 5.2 shows the initial conditions for reentry (end of coast) which includes the specified altitude to release the RVs. When deploying both RVs, it is assumed that they are released at the same time and that one is directed in another direction by changing the azimuth angle by 45 degrees.

Table 5.2: Initial conditions for reentry trajectory

Parameter	Value
h	328.1 kft
γ	-19.44 deg
β	-11.08 deg
v	25.96 kft/s
Latitude	40.79°S
Longitude	54.12°E

The results for the trajectory analysis for reentry is shown in Figure 5.7 and Figure 5.8. A summary of the impact parameters for the two RVs is shown in Table 5.3.

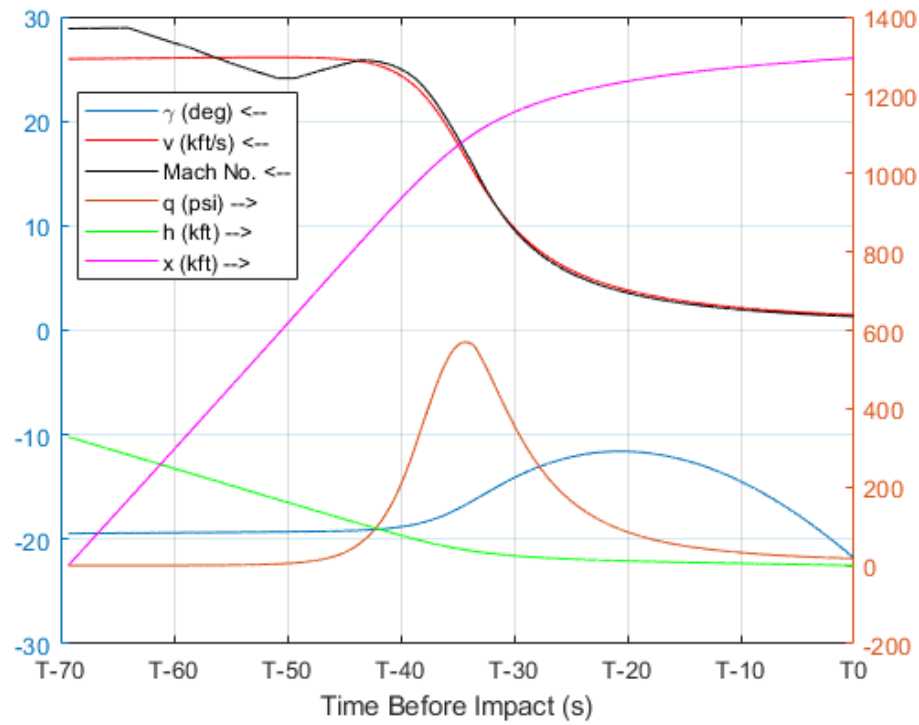


Figure 5.7: Time history of parameters for reentry trajectory

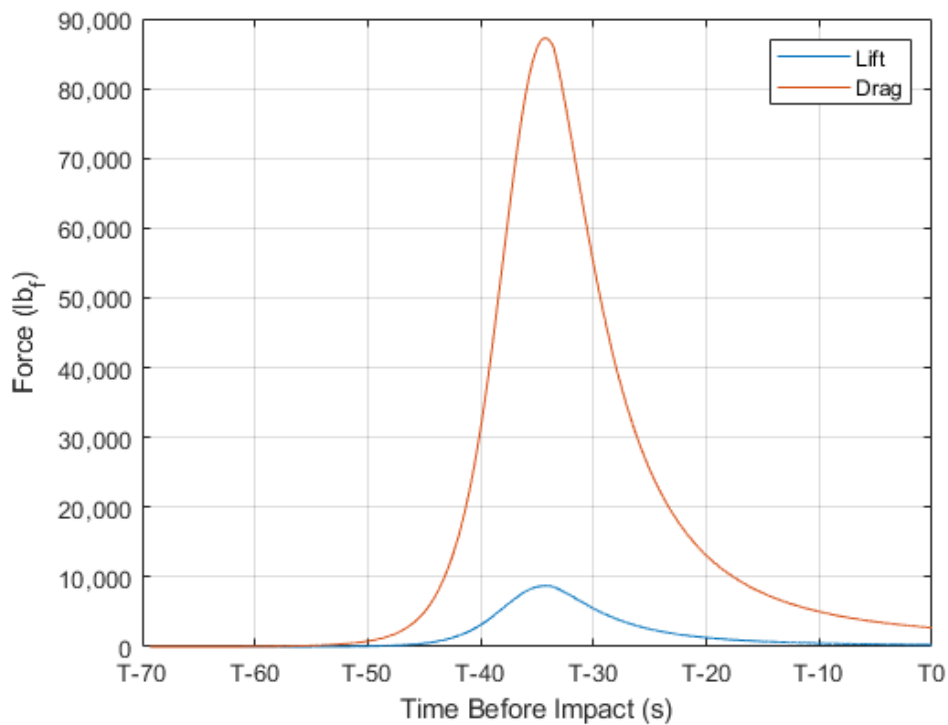


Figure 5.8: Time history of RV lift and drag forces

Table 5.3: Impact parameters for RVs

Parameter	RV #1	RV #2
Reentry Time	69.3 s	69.1 s
Impact velocity	1.470 kft/s	1.476 kft/s
Impact Mach No.	1.32	1.32
Flight path angle	-21.79 deg	-21.70
Latitude	40.79°S	39.25°S
Longitude	54.12°E	57.00°E

Something of note in Figure 5.7 is the sudden changes in Mach number. This is due to the change in atmospheric temperature from the standard atmosphere model. It can also be noted that the footprint between the two RVs is about 124 nmi which satisfies the requirement of having a footprint of at least 100 nmi.

5.2.3 Overall Trajectory Results

Having simulated the entire trajectory, the results can be combined to show how parameters vary throughout the duration of the mission. The key results of payload deployment time and range shown in Table 5.4 demonstrate that the design meets RFP requirements. The payload deployment time is within the 90 minute threshold while the range exceeds the objective range of 10,000 nmi.

Table 5.4: Key results for entire trajectory

Payload Deployment Time	74.28 min
Flight Time	75.43 min
Total Range	10,035 nmi

Additional results are plotted in Figure 5.9 and Figure 5.10. A 3-D view of the trajectory is shown in Figure 5.11. Figure 5.12 shows the ground track of the trajectory and also highlights the deployment of two RVs.

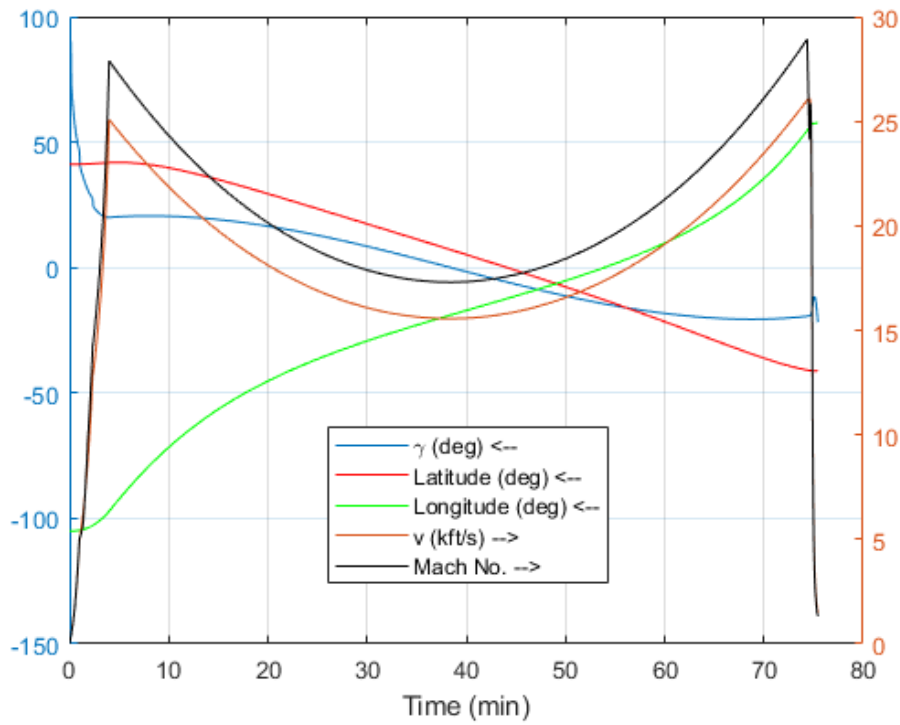


Figure 5.9: Time history of parameters for entire trajectory

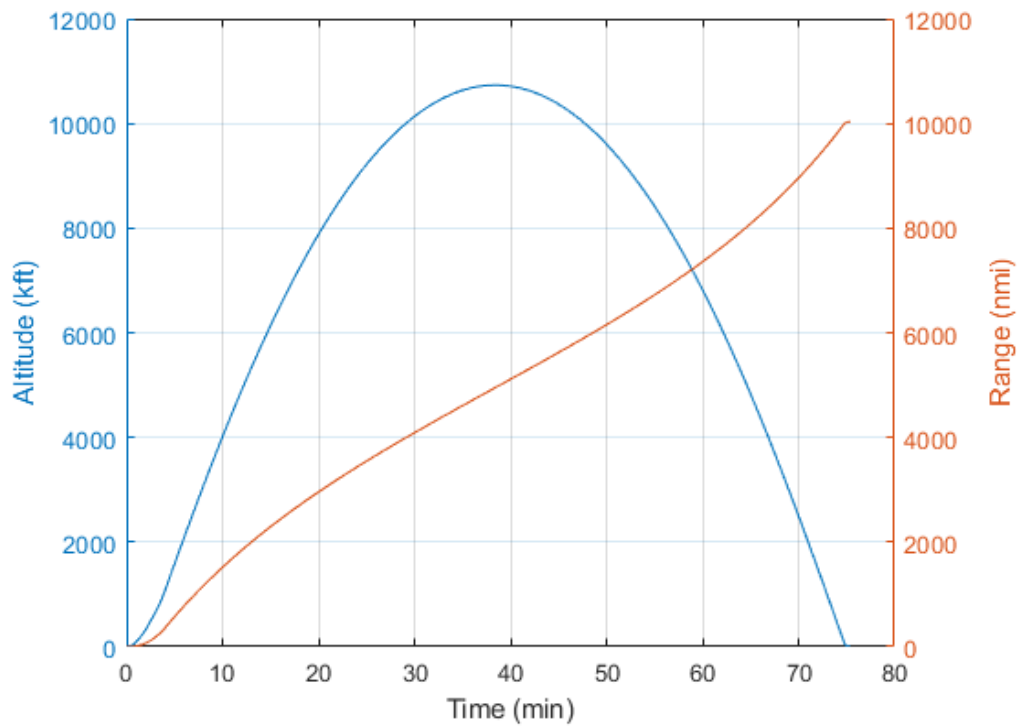


Figure 5.10: Time history of altitude and range for the entire trajectory

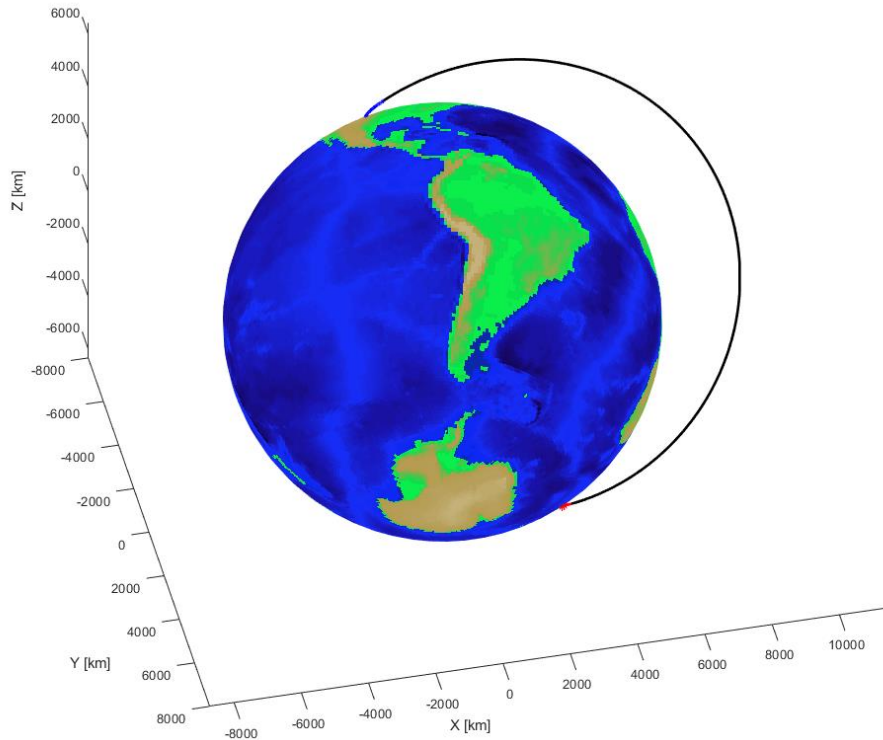


Figure 5.11: 3D Overview of Trajectory

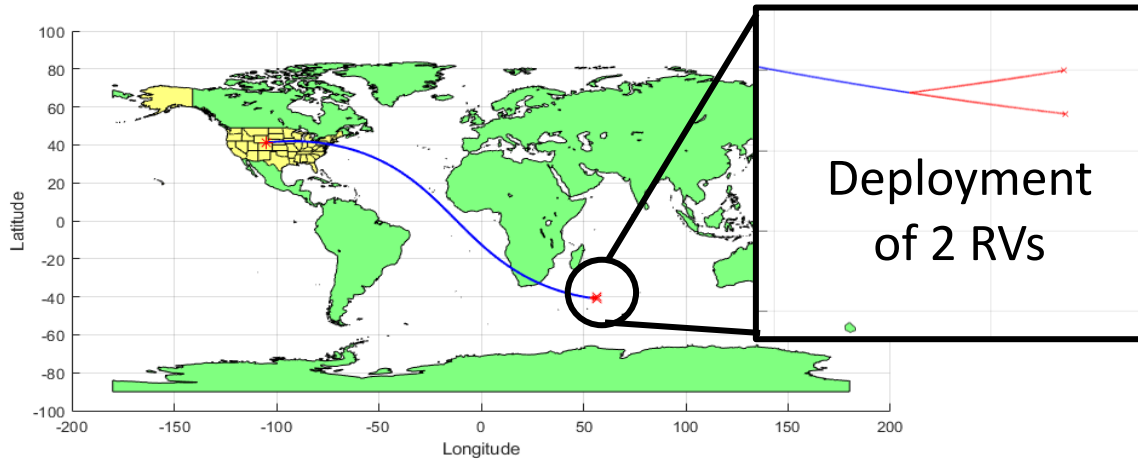


Figure 5.12: Ground Track of Trajectory

5.3 Reentry Heating

Thermal effects of atmospheric reentry were also analyzed using hypersonic flow past a flat plate.

Approximate convective heat transfer for the stagnation point and the surface of the RV were

obtained using the following relations from [17]. Note that variables in these equations must be in SI units (W/m^2 for q , m/s for V , and kg/m^3 for ρ).

$$q_w = \rho_{\infty}^N V_{\infty}^M C \quad (5.12)$$

The values for N , M , and C are defined in the following table.

Table 5.5: Values for estimating hypersonic aerodynamic heating

	N	M	C
Stagnation Point	0.5	3	$1.83 \times 10^{-8} R^{-0.5} \left(1 - \frac{h_w}{h_0}\right)$
Laminar Flat Plate	0.5	3.2	$2.53 \times 10^{-9} (\cos \phi)^{0.5} (\sin \phi) x^{-0.5} \left(1 - \frac{h_w}{h_0}\right)$
Turbulent Flat Plate ($V < 3962$ m/s)	0.8	3.37	$3.89 \times 10^{-8} (\cos \phi)^{1.78} (\sin \phi)^{1.6} x_T^{-1/5} \left(\frac{T_w}{556}\right)^{-1/4} \left(1 - 1.11 \frac{h_w}{h_0}\right)$
Turbulent Flat Plate ($V > 3962$ m/s)	0.8	3.7	$2.2 \times 10^{-9} (\cos \phi)^{2.08} (\sin \phi)^{1.6} x_T^{-1/5} \left(1 - 1.11 \frac{h_w}{h_0}\right)$

Finally, to estimate the temperature, the Stefan-Boltzmann law for a grey body was utilized.

$$q_w = \varepsilon \sigma T_w^4 \quad (5.13)$$

These equations are implemented within the trajectory code to determine the heat transfer of the RV during the entire reentry trajectory. Stagnation heat transfer is shown in Figure 5.13 and Figure 5.14 and the surface temperature distribution is shown in Figure 5.15. The maximum heat flux was found to be about $6,954 \text{ BTU/s-ft}^2$ and occurs at an altitude of 60.38 kft. Assuming an

emissivity of 0.75 for the RV material, the maximum nose or stagnation point temperature was calculated to be 11,357 deg F.

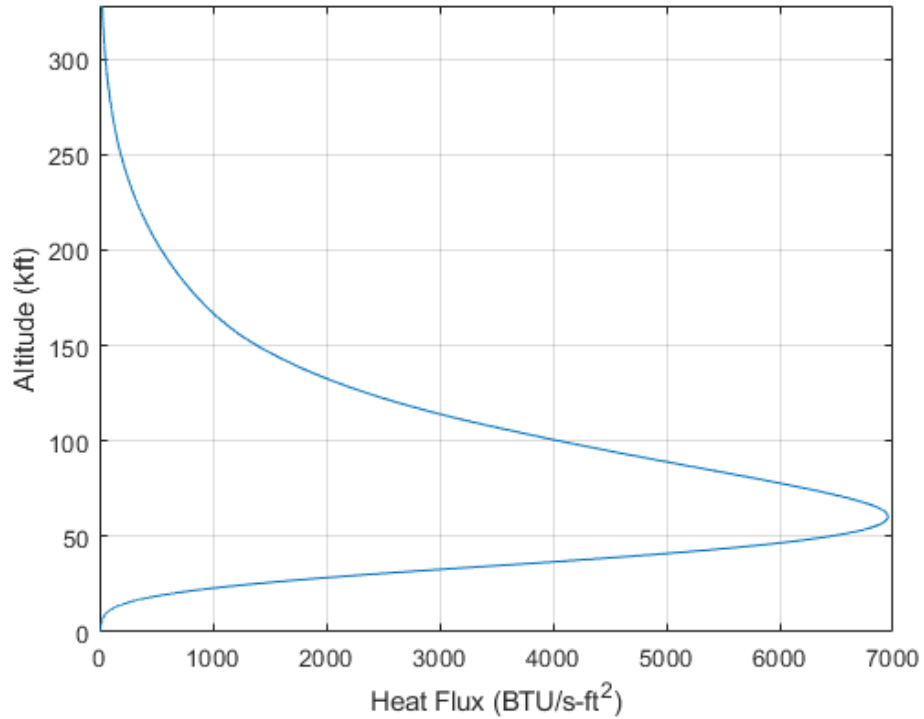


Figure 5.13: Stagnation point heat flux plotted against altitude

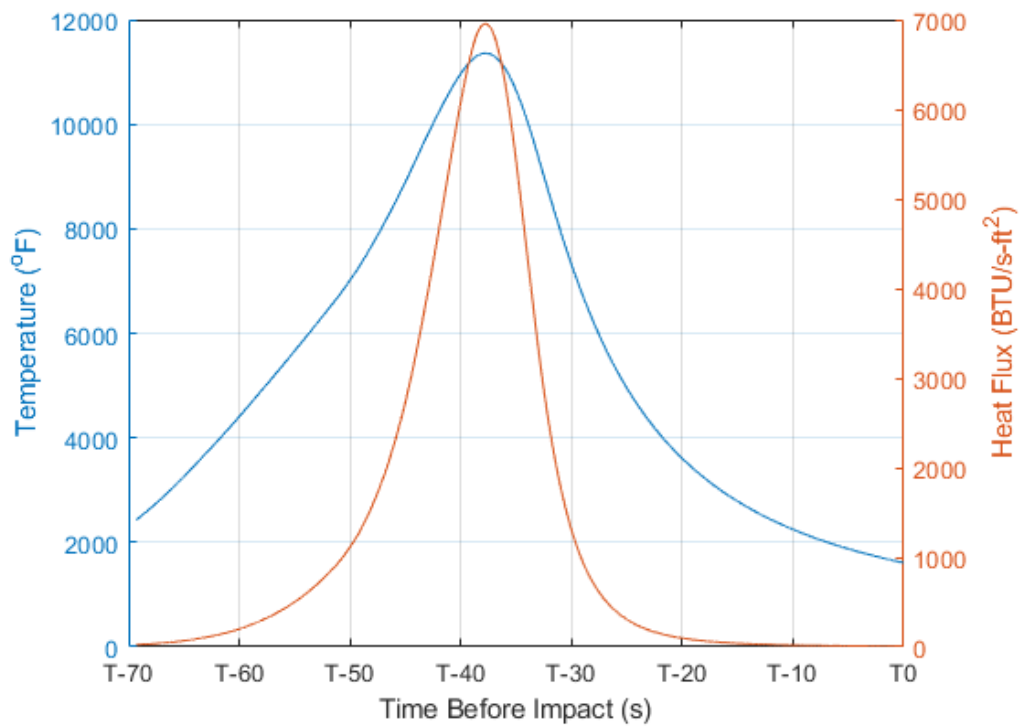


Figure 5.14: Stagnation temperature and heat flux versus time

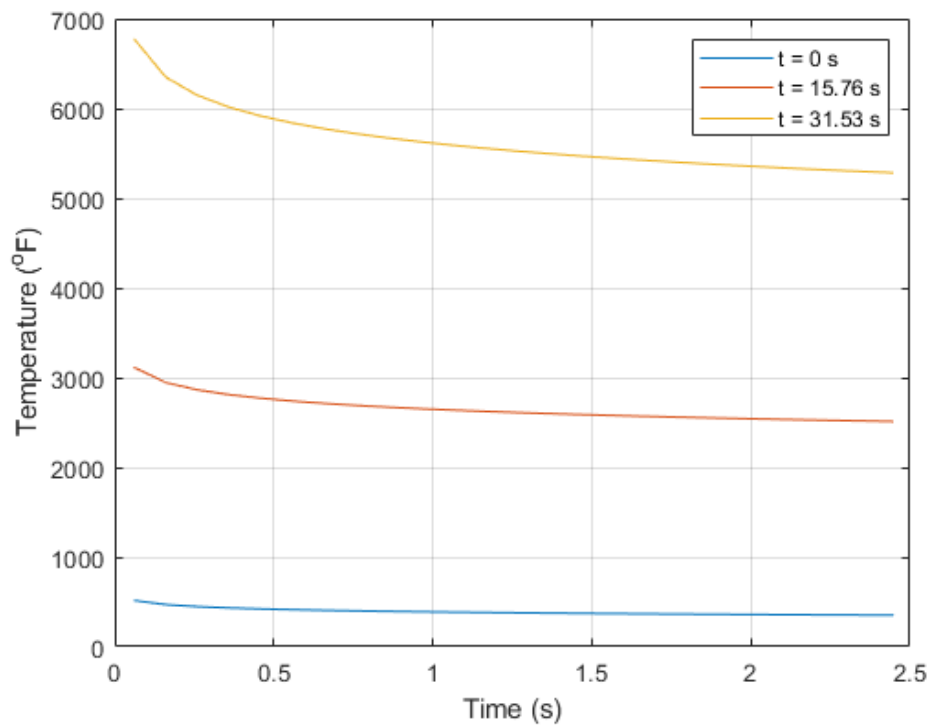


Figure 5.15: Temperature distribution of RV surface at select times into reentry flight

The required insulation thickness for the RV was calculated with equation from [18].

$$\frac{T(x,t)-T_a}{T_i-T_a} = \operatorname{erf}\left(\frac{x}{2\sqrt{\alpha t}}\right) \quad (5.14)$$

It is assumed that the ablative insulation material for the RV is silica phenolic & fiberfrax preform with material properties taken from [18]. The estimated time of heating above the ablation temperature of 4040 F was determined to be about 40 seconds from the analysis performed earlier. Using an initial temperature of 80 F for the RV and a maximum allowable temperature of 260 F resulted in a minimum insulation thickness of 0.386 inches.

5.4 Circular Error Probable

Circular error probable (CEP) is defined as the radius of a circle centered on the impact point of the nominal trajectory where 50 percent of the trajectories impact within the radius. In order to determine the CEP, the downrange and cross-range errors must be accounted for through statistical analysis or Monte Carlo simulations. The latter method was chosen, as it could be easily implemented into the existing MATLAB code for the reentry trajectory. The standard deviations are obtained for each of the errors and used in the following equations provided by [19].

$$CEP = \sigma_{max} \left\{ 0.674 \left(\frac{\sigma_{min}}{\sigma_{max}} \right) \left[0.0786 + 0.2573 \left(\frac{\sigma_{min}}{\sigma_{max}} \right) + 1.1108 \left(\frac{\sigma_{min}}{\sigma_{max}} \right)^2 \right] \right\} \text{ for } \quad (5.15)$$

$$0.0 < \sigma_{min}/\sigma_{max} \leq 0.35$$

$$CEP = 0.562\sigma_{max} + 0.615\sigma_{min} \text{ for } 0.35 < \sigma_{min}/\sigma_{max} \leq 1.0 \quad (5.16)$$

The atmospheric density and initial reentry conditions were randomly varied to determine difference between actual impact point and nominal impact point. Parameters varied include velocity, altitude, azimuth angle, flight path angle, and atmospheric density. In doing so, the tolerances required to meet the CEP requirements were determined for the various flight parameters.

Using the reentry parameters from before and performing 100,000 simulations, a CEP of 130 ft was achieved with the tolerances summarized below in Table 5.6.

Table 5.6: Summary of CEP tolerances for RV initial conditions

Velocity / Altitude	$\pm 0.01 \%$
Flight Path Angle	$\pm 0.001 \%$
Azimuth Angle	$\pm 0.1 \%$
Atmospheric Density Variation	$\pm 0.2 \%$

Figure 5.16 below shows the results of 500 runs. Note that, when 100,000 simulation were conducted, the CEP expanded to roughly 135 ft. This falls within the threshold requirement of 150 ft.

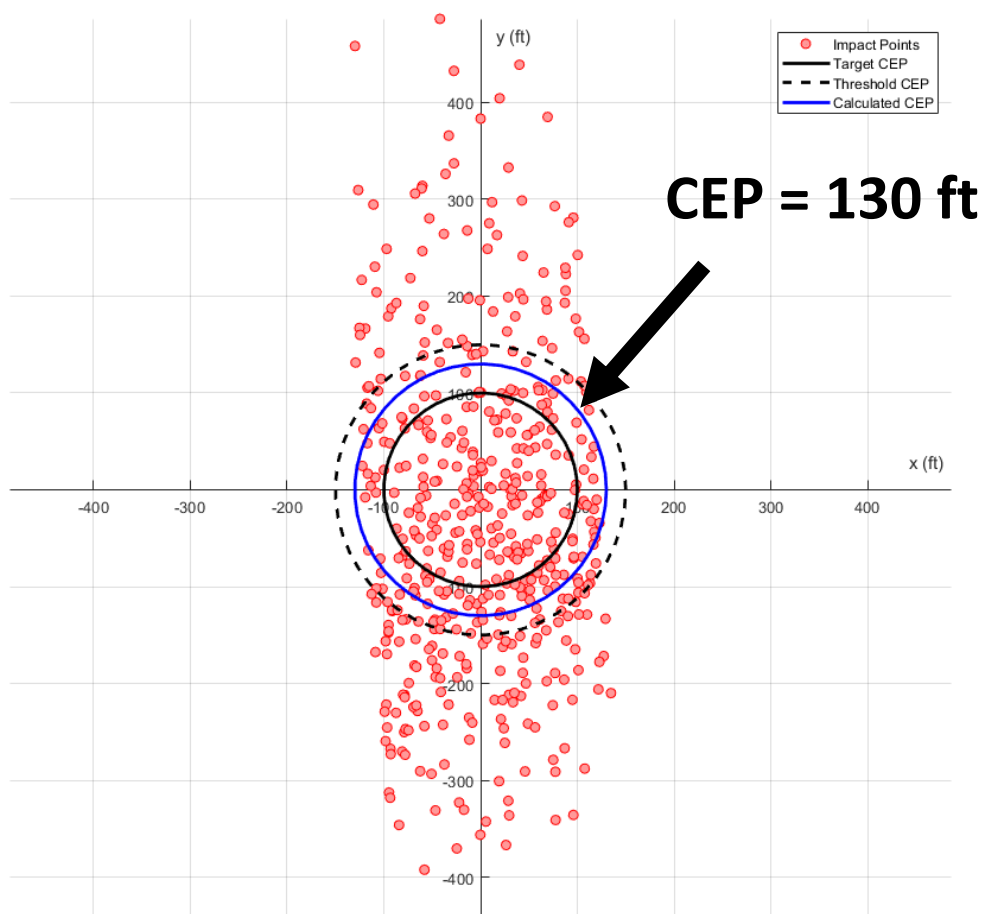


Figure 5.16: CEP results for 500 simulations

6 Structural Analysis

Nomenclature

Symbols

A	=	Side area
A _x	=	Axial force
C _D	=	Drag coefficient
D	=	Drag
L	=	Lift
m	=	Mass
M	=	Moment
q	=	Dynamic pressure
r	=	Fuselage radius
t	=	Fuselage thickness
v	=	Velocity
v _w	=	Velocity of wind
V	=	Shear force

Greek Letters

α	=	Instantaneous angle of attack
σ	=	Stress

Structural analysis was conducted by analyzing flight conditions at maximum dynamic pressure (max q). The aerodynamic forces were calculated at these conditions and used to ascertain the load profile throughout the length of the vehicle. From this, the relevant stresses were calculated, and margins of safety were assessed. All equations were taken from the course text [7] [20].

6.1 Ground Loads

Ground loads were assessed with the assumption that the vehicle is sitting in the silo. This means that there are no wind forces to be considered, and only the axial load due to the weight of the vehicle is what must be analyzed.

To conduct this analysis, the total weight of each component of the vehicle were calculated (based on results from inboard profile sizing). The weights were then added along the length of the vehicle such that they naturally compound towards the bottom. The results of this analysis are

summarized below in Table 6.1 and Figure 6.1. The maximum axial force experienced is 2655 kips, located at the bottom of the vehicle.

Table 6.1: Ground Axial Loads

Item	Mass (lb)	Axial Load (kips)	Total Axial Load (kips)
Solid Rocket Motor	5269	169.6	2655
Gimbals Stage 1	25	0.8	2485
Thrust Structure Stage 1	436	14.1	2484
Aft Skirt	160	5.2	2470
SRB Tank	110	3.5	2465
Propellant Stage 1	37648	1212.3	2461
Stg 1 Dome Cover	96	3.1	1249
Stage 1/2 Interstage	271	8.7	1246
Engine Stage 2	950	30.6	1237
Gimbals Stage 2	30	1.0	1207
Thrust Structure Stage 2	202	6.5	1206
Fuel Tank Stage 2	132	4.2	1199
Fuel Stage 2	13755	442.9	1195
Wiring	941	30.3	752
Stage 2 Intertank	169	5.4	722
Oxidizer Tank Stage 2	99	3.2	716
Oxidizer Stage 2	8488	273.3	713
Stage 2/3 Interstage	154	5.0	440
Engine Stage 3	517	16.7	435
Gimbals Stage 3	6	0.2	418
Thrust Structure Stage 3	68	2.2	418
Fuselage Dome Cover	45	1.4	416
Oxidizer Tank Stage 3	93	3.0	414
Oxidizer Stage 3	7750	249.5	411
Stage 3 Fuselage	156	5.0	162
Fuel Tank Stage 3	33	1.1	157
Fuel Stage 3	1389	44.7	156
Upper Attachment	29	0.9	111
Avionics	955	30.8	110
Payload	2200	70.8	79
Fairing	265	8.5	9

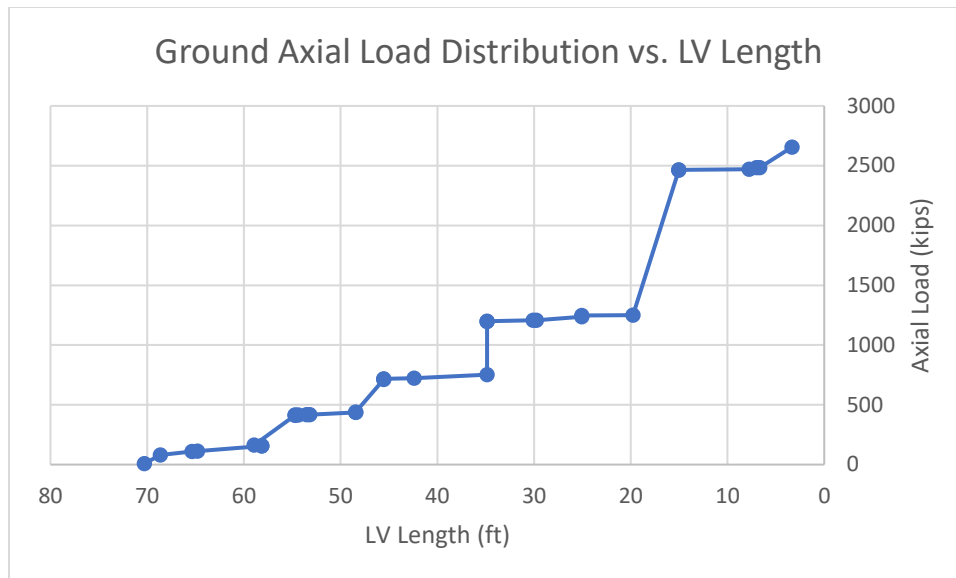


Figure 6.1: Ground Axial Load Distribution

6.2 Max q Data

Max q represents the point at which the vehicle experiences the most intense aerodynamic loads and is therefore a good benchmark to verify the integrity of the vehicles structure. The important max q parameters were extracted from the trajectory simulation (see section 5.0) and are summarized below in Table 6-2.

Table 6.2: Max-q Parameters

q_{max}	14.07	psi
Mass at q_{max}	51,127	lb _m
C.G. at q_{max}	40.3	ft
Mach Number	2.474	-
v	2,395	ft/s
h	36,149	ft

Next, the instantaneous angle of attack (α) must be calculated based on the horizontal wind gusts acting on the vehicle. This is found by vectorially adding the sideways wind gust to the vehicle velocity and using the trigonometric relation shown below in equation 6.1.

$$\alpha = \tan^{-1}\left(\frac{v_w}{v}\right) \text{ for} \quad (6.1)$$

The wind gust velocity, v_w , was found in a winds-aloft chart provided in the course text. With this chart, the wind gust speed may be assessed based on altitude. With a v_w of about 95 ft/s, the instantaneous angle of attack was calculated to be $\alpha = 2.54^\circ$.

6.3 Calculation of Load Distributions

To calculate the loads at max q , several key assumptions were made. First, it was assumed that all external portions of the fuselage possessed a constant drag coefficient of $C_D = 0.7$. Next, it was established that only the fairing and the tapered fuselage portions of the vehicle produced a considerable amount of lift, while the cylindrical (constant diameter) portions produced a negligible amount. The required coefficients of lift were calculated based on geometry and relevant experimental data found in the course text. Finally, the lift and drag forces were calculated for each portion of the fuselage with equations 6.2 and 6.3.

$$L_i = C_{L_i} q A_i \quad (6.2)$$

$$D_i = C_{D_i} q A_i \quad (6.3)$$

Where A_i is the side area and q is the maximum dynamic pressure shown in the previous subsection.

The lift and drag components were then converted into body coordinates perpendicular and parallel to the length of the vehicle. These body coordinates are represented by shear and axial forces and were calculated equations 6.4 and 6.5.

$$V_i = L_i \cos\alpha + D_i \sin\alpha \quad (6.4)$$

$$Ax_i = D_i \cos\alpha - L_i \sin\alpha \quad (6.5)$$

Where α is the instantaneous angle of attack calculated with the winds aloft chart in the previous sub-section. A chart breaking down the shear and axial loads throughout the vehicle is shown below in Table 6-3. Note that this only accounts for the external portions of the vehicle.

Table 6.3: Vehicle Max-q Flight Loads

Item	Lift L (lbf)	Drag D (lbf)	Shear, V (lbf)	Axial, A (lbf)
Solid Rocket Motor	0	37514	1662	37477
Aft Skirt	0	42041	1863	42000
SRB Tank	0	74995	3324	74921
Stg 1 Dome Cover	0	26298	1165	26272
Stage 1/2 Interstage	4922	64591	7779	64745
Fuel Tank Stage 2	0	76733	3401	76657
Stage 2 Intertank	0	44187	1958	44144
Oxidizer Tank Stage 2	0	6572	291	6565
Stage 2/3 Interstage	3097	37109	4739	37210
Fuselage Dome Cover	0	11694	518	11682
Oxidizer Tank Stage 3	0	15988	709	15972
Stage 3 Fuselage	0	41012	1818	40972
Upper Attachment	0	7717	342	7710
Fairing	5401	33074	6861	33281

After converting everything into body coordinates, the total moment about the center of gravity may be assessed. The net moment is then balanced by an assumed engine gimbaling force at the nozzle of the first stage.

Additionally, the net lateral load is calculated, and the resultant lateral acceleration is found with Newton's second law. With this, the inertial relief forces throughout the *entire* vehicle due to d'Alembert's principle may be calculated and added to the previously found forces. With all the possible loads calculated, the total shear, axial, and moment distributions were tabulated. This is shown below in Table 6.4.

Table 6.4: Total Shear, Axial, and Moment Distributions

Item	Total Shear Load (lbf)	Total Axial Load (lbf)	Total Bending Moment (lbf-ft)
Solid Rocket Motor	-12086	576595	35640
Gimbals Stage 1	-9363	533849	36719
Thrust Structure Stage 1	-9342	533824	36719
Aft Skirt	-8979	533388	36755
SRB Tank	-10709	491227	34420
Propellant Stage 1	-13941	416196	26819
Stg 1 Dome Cover	-10262	404005	38585
Stage 1/2 Interstage	-3793	377637	37710
Engine Stage 2	-11347	312621	20866
Gimbals Stage 2	-10556	311670	21685
Thrust Structure Stage 2	-10531	311640	21685
Fuel Tank Stage 2	-10363	311438	21702
Fuel Stage 2	-13654	234649	11999
Wiring	-2205	220894	28715
Stage 2 Intertank	-1422	219953	28715
Oxidizer Tank Stage 2	-3240	175640	25561
Oxidizer Stage 2	-3449	168977	25499
Stage 2/3 Interstage	3615	160489	26377
Engine Stage 3	-995	123124	19225
Gimbals Stage 3	-564	122607	19549
Thrust Structure Stage 3	-559	122601	19549
Fuselage Dome Cover	-503	122534	19554
Oxidizer Tank Stage 3	-984	110807	19289
Oxidizer Stage 3	-1615	94741	18804
Stage 3 Fuselage	4835	86992	21142
Fuel Tank Stage 3	3148	45863	17883
Fuel Stage 3	3175	45830	17898
Upper Attachment	4332	44441	18536
Avionics	4014	36702	18421
Payload	4809	35747	18421
Fairing	6640	33547	20252
Tip of LV	0	0	0

These distributions are also shown below in Figure 6.2, 6-3, and 6-4. Note how they are balanced at each end of the vehicle due to the engine gimbal. Additionally, the effects of the tapered diameters on the loads are easily observable.

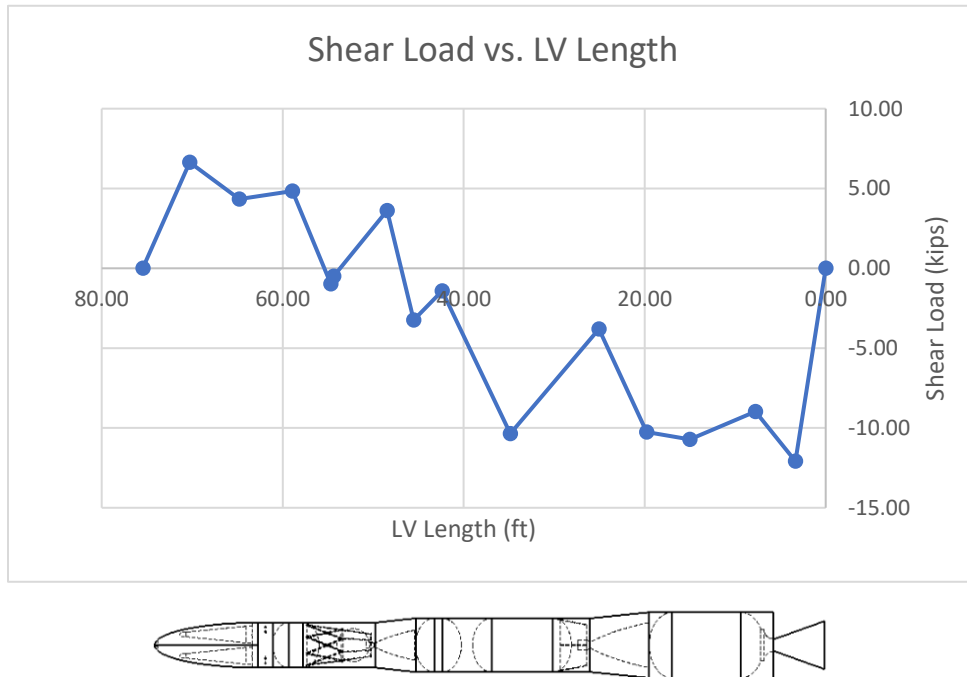


Figure 6.2: Max-q Shear Load Distribution

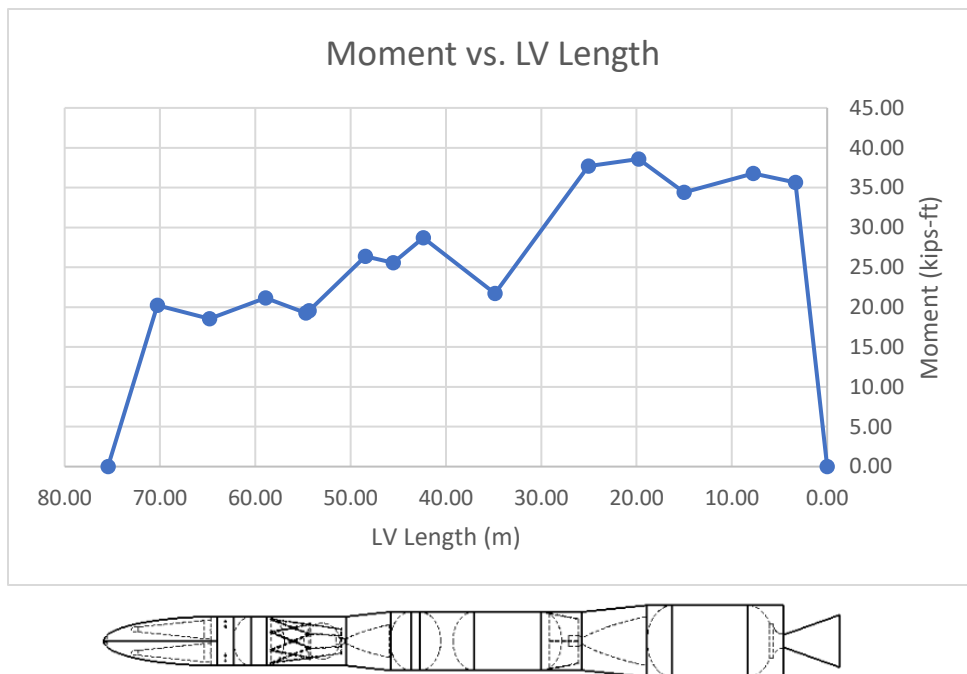


Figure 6.3: Max-q Moment Distribution

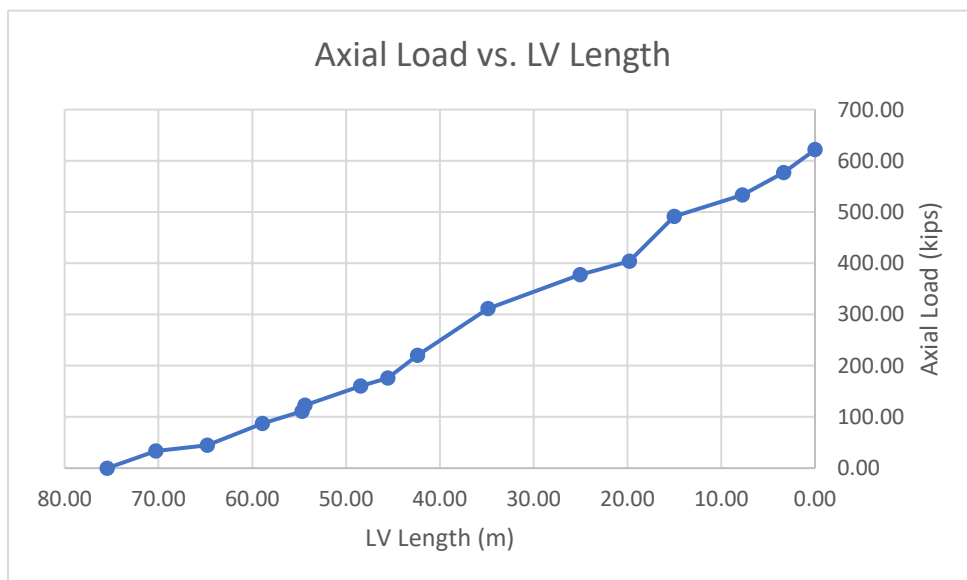


Figure 6.4: Max-q Axial Load Distribution

6.4 Stress Analysis

With the load distributions, the maximum stresses throughout the vehicle may be calculated. First, it was assumed that the structural components may be simplified into hollow cylinders made of Al 2219 with a minimum thickness of 0.06 inches.

The maximum stress was calculated based on a combination of axial and bending stress, shown below in equation 6.6

$$\sigma_{max} = |\sigma_{axial}| + |\sigma_{bending}| = \frac{Ax}{\pi r^2} + \frac{M}{\pi r^2 t} \quad (6.6)$$

After calculating the maximum stress for each component of the vehicle, it was then compared to the yield strength of the material ($F_{ty-Al\ 2219} = 57\ ksi$) [20] to find the margin of safety. Throughout the analysis, the vehicle was designed for a minimum margin of safety of 1.5.

Table 6.5 summarizes the results of the stress analysis.

Table 6.5: Stress Analysis Summary

Item	Max Stress (ksi)	M.S.
Solid Rocket Motor	39.91	4.46
Aft Skirt	37.35	1.53
SRB Tank	34.46	5.16
Stg 1 Dome Cover	29.51	1.93
Stage 1/2 Interstage	27.77	2.05
Fuel Tank Stage 2	27.36	2.08
Stage 2 Intertank	21.58	2.64
Oxidizer Tank Stage 2	17.68	3.22
Stage 2/3 Interstage	16.66	3.42
Fuselage Dome Cover	15.94	3.58
Oxidizer Tank Stage 3	14.81	3.85
Stage 3 Fuselage	13.09	4.36
Upper Attachment	8.57	6.65
Fairing	7.99	7.13

7 Guidance, Navigation, and Controls

Assessing the initial stability of the rocket was done so by developing a root locus with no controller implemented. This was done so by looking at the moment differential equation based on the thrust and lateral force found when assessing flight loads. Applying a Laplace transform of that differential and solving in terms of the relation of output to input, a plant transfer function was formulated. Finally, the root locus of this transfer function was assessed for stability, and a PID controller was applied for increase stability and more desirable system response characteristics.

7.1 Initial Stability Estimation

The transfer function of the plant with no controller implemented is shown below:

$$sys = \frac{8.214e5}{1.897e5 s^2 - 8.071e5} \quad (7.1)$$

Plotting the root locus of the transfer function yields that the rocket is marginally as there are two poles evenly spaced from the imaginary axis at ± 2.06 . The pole on the right-hand side of the root locus, as seen in Figure 6.1-1 will cause an exponential increase in error, creating the need for the implementation of a controller.

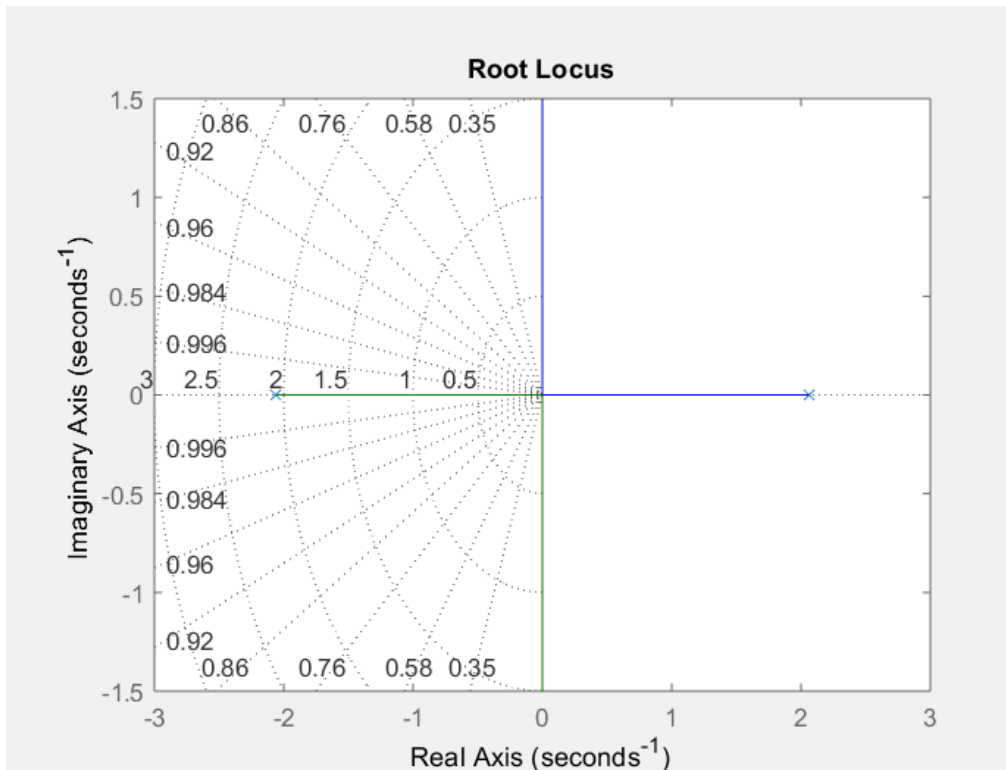


Figure 7.1: Root locus with no controller implemented

Additionally, the transfer function also yields the natural frequency to be 2.06 Hz, and time to double was found to be 0.61 seconds; this is considered to be stable as time to double should be greater than 0.5 seconds.

7.2 Implementation of PID Controller

A PID controller was implemented on the system to improve the system response. The controller was auto tuned in MATLAB, the criteria for the new system was response was >10% overshoot, >1 second settling time, and >5% steady state error.

All criteria were met as the overshoot was reduced to 3.1%, and settling time reduced to 0.117 seconds. The implementation of the controller also successfully moved the system

response to the stable side (left-hand plane), meaning error will decay with time. The new root locus and step response can be seen below in Figure 7.2 and Figure 7.3 respectively.

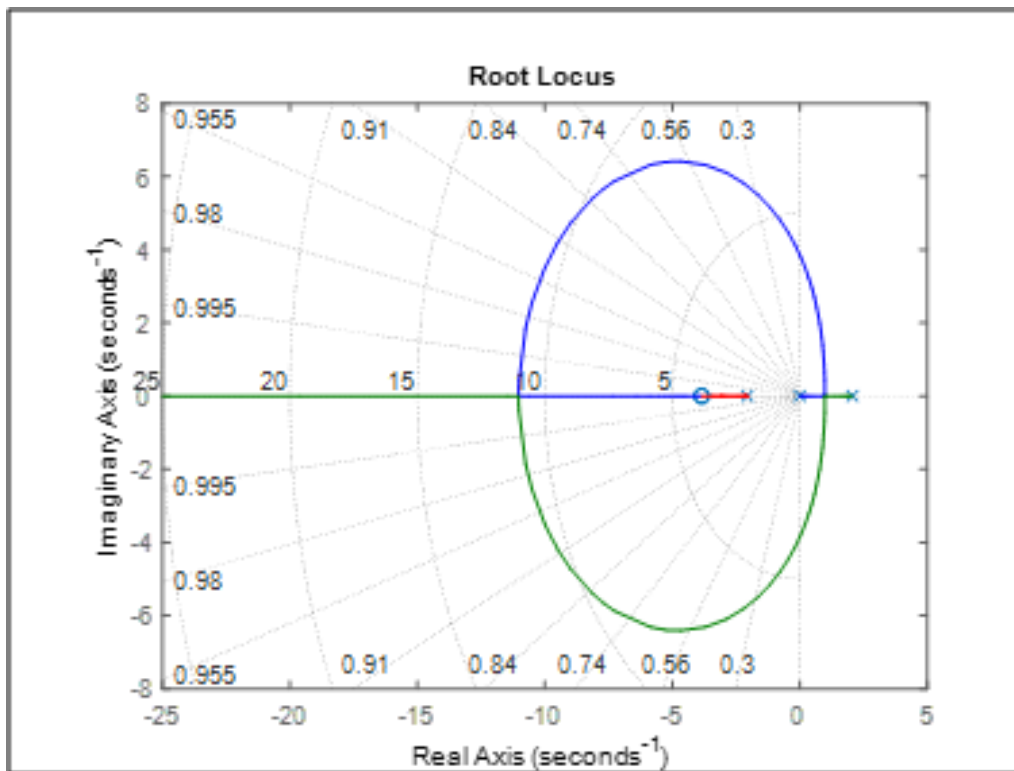


Figure 7.2: Root locus with PID controller implemented

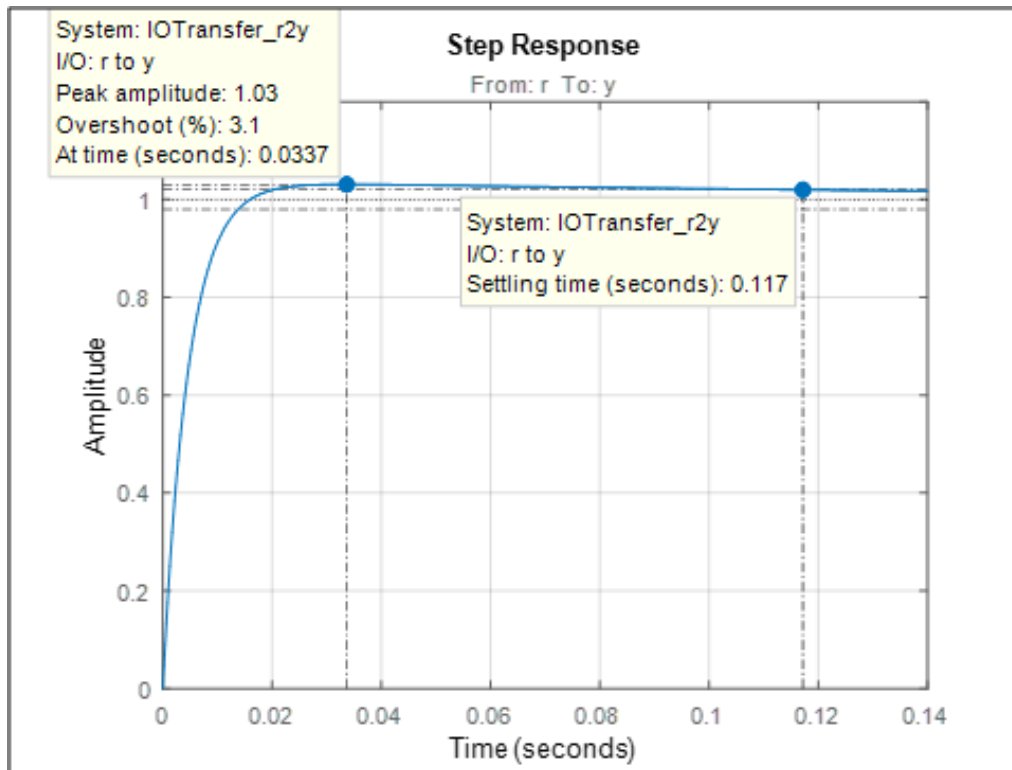


Figure 7.3: System response to step input

A basic block diagram of the system can be shown below; Figure 6.2-3 displays a general overview of the PID controller, thrust vectors, and sensors with respect to the plant.

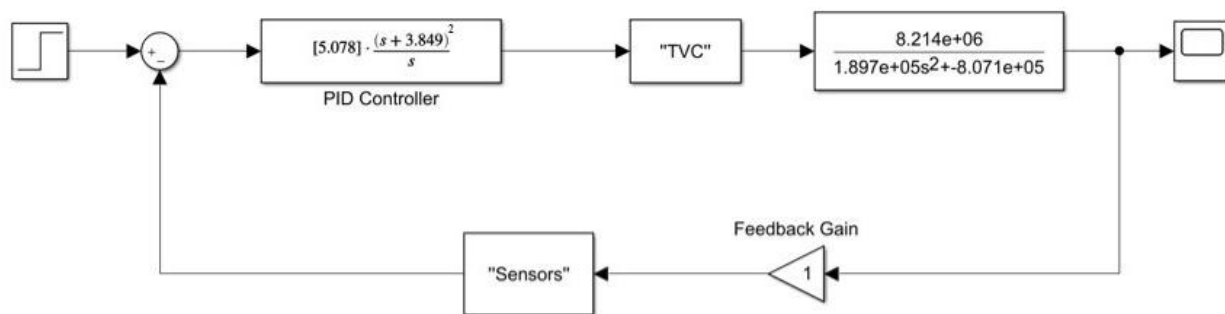


Figure 7.4: Block diagram for system with a PID controller

To meet the requirement of the use of celestial navigation, the vehicle will use and IMU and GPS as the sensors. The GPS works as standard, to record and display positioning, velocity and time computation. The IMU will account for all axis when looking at both positioning and

angular velocity. Together these six readings give an attitude calculation which is then compared to both the desired and the previous attitude readings. If desired positioning is not met, signal is sent to the actuators if desired positioning is not met. A detailed block diagram of the sensor-actuator system is shown in Figure 7.5.

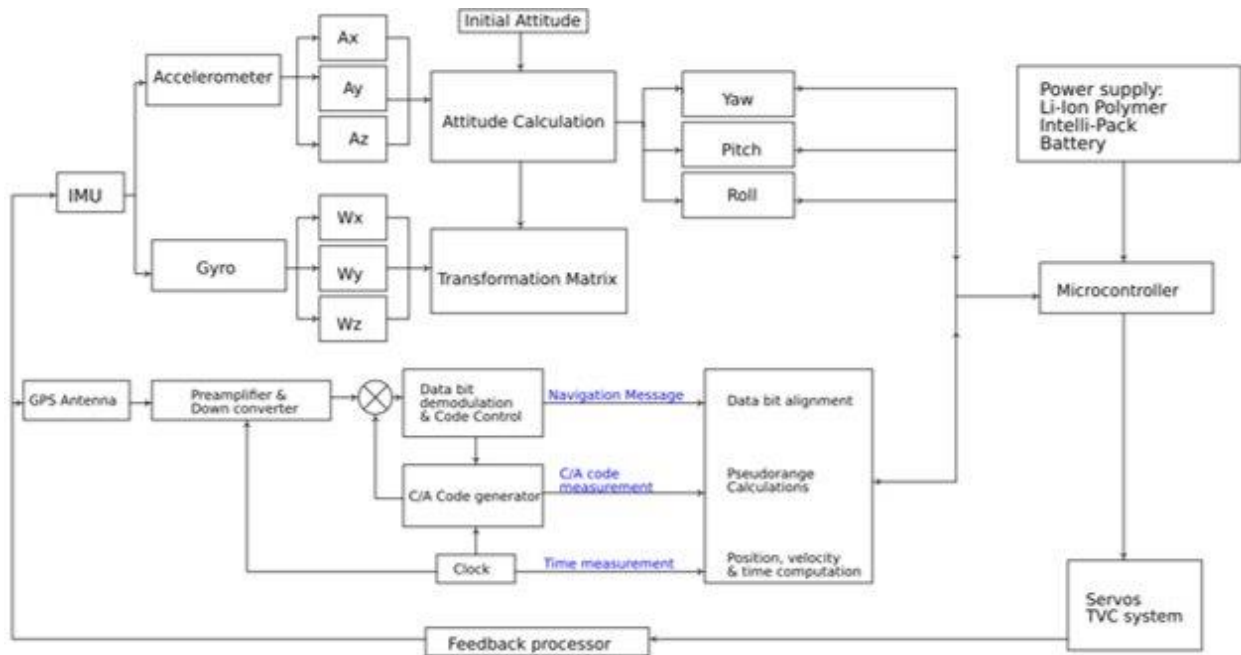


Figure 7.5: Detailed block diagram of sensor-actuator system

7.3 Frequency Analysis

The final stability analysis conducted was the frequency analysis to ensure that operating frequencies would not match the natural frequency to avoid resonance. The natural frequency was previously found using the transfer functions, the operating frequency was assessed for first and second bending modes. This analysis was conducted through FEMAP by modeling the entire rocket as a hollow cylinder and estimating the entire body to be made of Al 2219. The analysis yielded that the first and second bending modes are 4.60 Hz and 27.6 Hz respectively. From this it can be concluded resonance will not occur.

8 Hypersonic Glide Vehicle Design and Analysis

The hypersonic glide vehicle is an artifact from the second architecture briefly mentioned in section 2. However, it is still being considered for use with the current missile design if needs ever change or to provide more options to the customer for warhead delivery.

The HGV performs its mission by being launched to Earth's upper atmosphere at hypersonic speeds and gliding to the target [21]. Given that the HGV is a glider, the vehicle will typically not contain its own propulsion system; however, it is possible to include one for attitude control. Additionally, control surfaces would also be used for the HGV to maneuver during its flight towards the target. The HGV will be designed as a waverider to take advantage of the aerodynamic characteristics this vehicle class has in the hypersonic flight regime.

8.1 Waverider Design

A waverider is a point-designed vehicle based on a known flow field. They are designed for a specific Mach number and the resulting design is dependent on the shock angle and chosen shape for the flow field. For this analysis, a conical-derived waverider was chosen. Axisymmetric supersonic flow around a cone can be defined by the Taylor-Maccoll equation shown as follows.

$$\frac{\gamma - 1}{2} \left[1 - V_r^2 - \left(\frac{dV_r}{d\theta} \right)^2 \right] \left[2V_r + \frac{dV_r}{d\theta} \cot \theta + \frac{d^2V_r}{d\theta^2} \right] - \frac{dV_r}{d\theta} \left[V_r \frac{dV_r}{d\theta} + \frac{dV_r}{d\theta} \frac{d^2V_r}{d\theta^2} \right] = 0 \quad (8.1)$$

This ordinary differential equation must be solved numerically and is done so by using ode45 in MATLAB. The specific heat ratio, Mach number, and shock angle are used as the initial conditions. The output from solving the equation is obtaining the cone angle and flow properties after the shock. Streamlines are then traced behind the shockwave to form the lower compression surface of the waverider as shown in Figure 8.1. From there, the upper surface of the waverider is

defined by the freestream flow. After defining both surfaces, this completes the design of a waverider for inviscid flow.

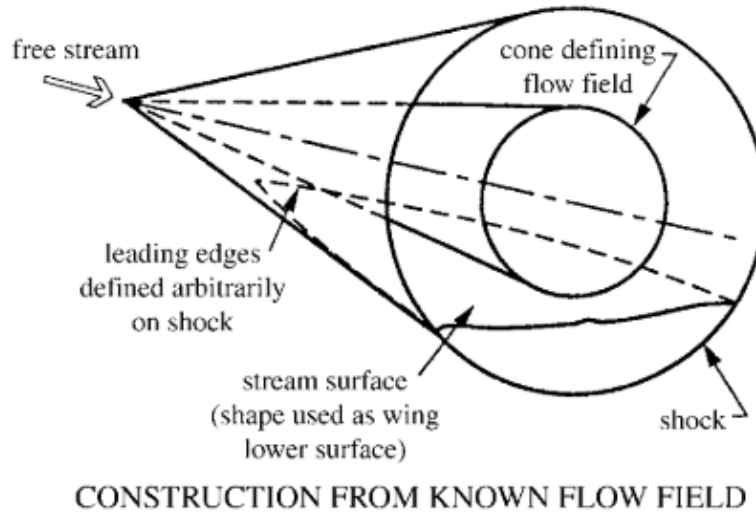


Figure 8.1: Streamline tracing to form the compression surface of a waverider [17]

A design method proposed by Bowcutt [22] and Corda [23] lay out a process to optimize a waverider to either maximize L/D or minimize drag while accounting for viscous flow effects. Figure 8.2 provides an overview of the iterative optimization process.

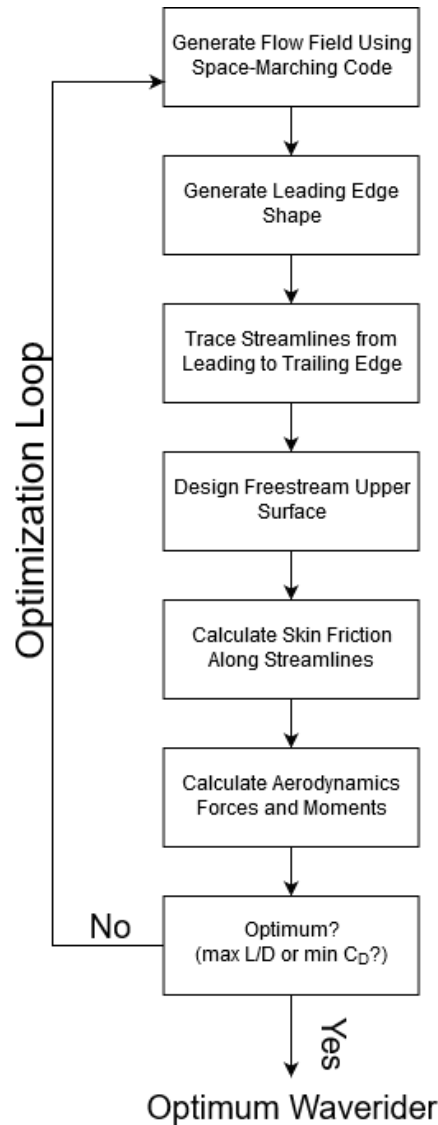


Figure 8.2: Optimization process to design a viscous optimized waverider. Original illustration from [23]

Due to time constraints, the optimization process for a viscous optimized waverider design could not be implemented for the HGV design.

8.1.1 Geometric Relations

In order to have a capability for rapid generation of different designs for the HGV, geometric relations were utilized. A method of generating the upper surface is provided by [24]. The coordinate system for this method is centered at the vertex of the cone with the positive z-axis in

the direction of the base of the cone. The lower surface is generated by using the method described in [25] and is adapted to use the same coordinate system as [24]. These methods are implemented into a MATLAB code to produce the x , y , z points that can be imported into SolidWorks to generate a CAD model of the waverider.

An example of waverider designed for Mach 20, a shock angle of 30 degrees, and a 150 in long cone is shown in Figure 8.3 and Figure 8.4.

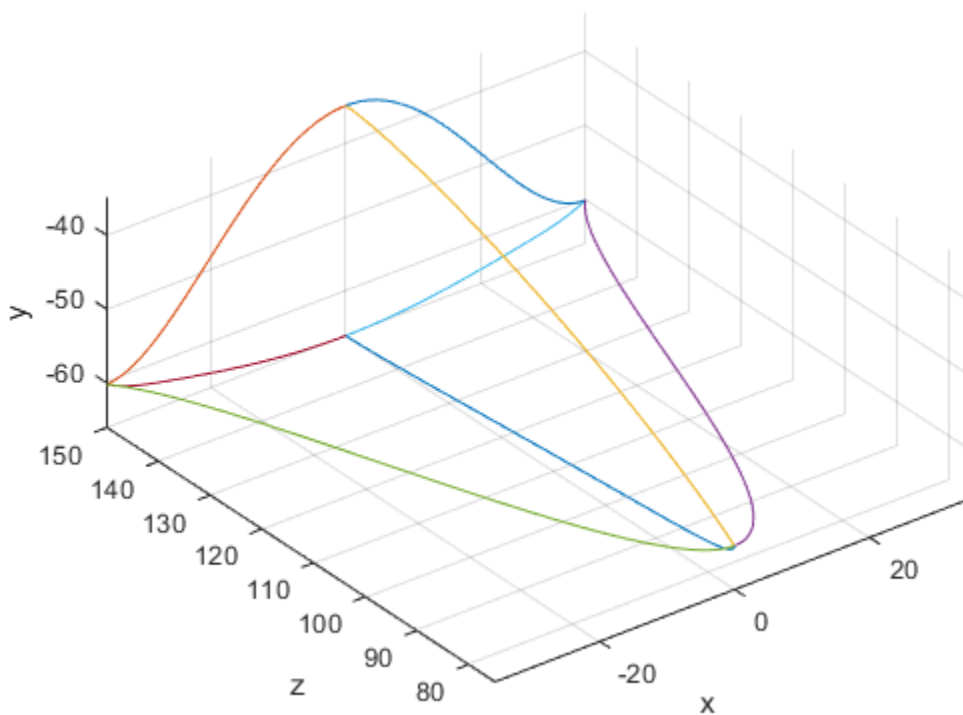


Figure 8.3: MATLAB output of waverider shape in inches

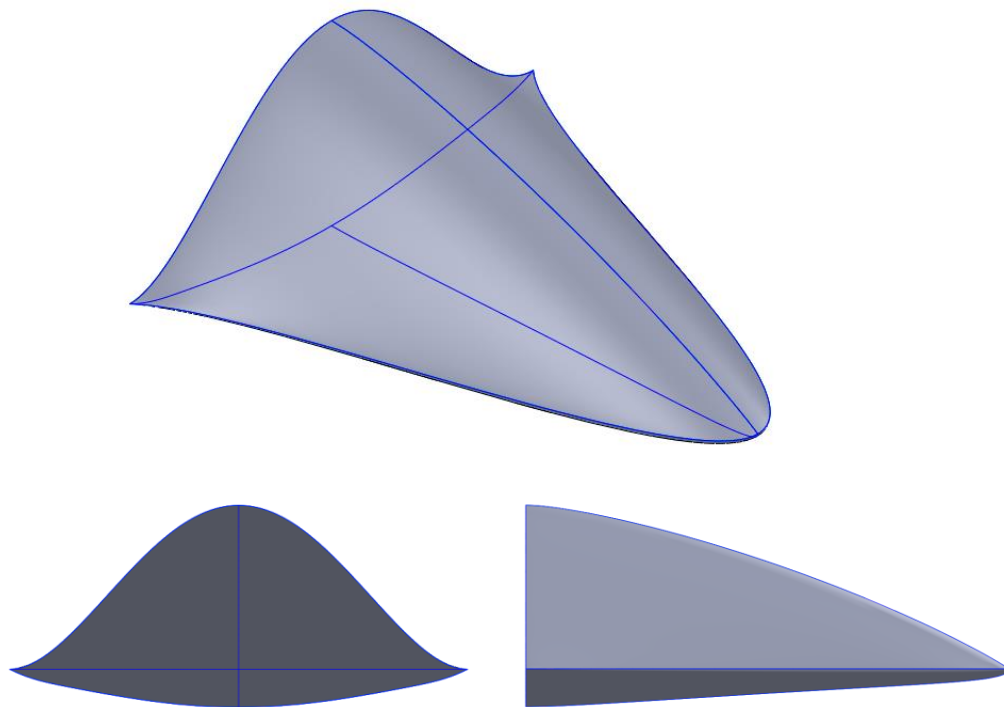


Figure 8.4: 3-view diagram of HGV CAD model

This design tool allows for easy generation of a shape that can be rapidly iterated to fit the needs of the size and trajectory requirements.

8.2 HGV Trajectory

The trajectory modeling of the HGV follows the same approach as the reentry vehicle described in section 5. The major difference is that the L/D of HGV plays a prominent role in how far downrange the vehicle can deliver the payload. Additionally, the HGV can perform midflight maneuvers by changing the bank (roll) angle. The initial conditions for the HGV trajectory are assumed values and are shown in Table 8.1. The maneuvers that the HGV performs throughout its trajectory are outlined in Table 8.2.

Table 8.1: Initial conditions for HGV trajectory

Parameter	Value
h	656.2 kft
γ	-1 deg
β	0 deg
v	22.97 kft/s
Latitude	40°N
Longitude	85°W

Table 8.2: HGV maneuvers

Bank Angle (deg)	Time Span (s)
0	0 – 500
-10	500 – 1500
20	1500 – end

Additionally, the following values were assumed: $C_D = 0.3$, $L/D = 2.5$, $m = 10,000 \text{ lb}_m$. The lift to drag ratio was chosen based on analysis done for the Hypersonic Technology Vehicle-2 (HTV-2) in [26]. These parameters were then inputted into the MATLAB trajectory code to produce trajectory of the HGV to impact. Figure 8.5 shows the time history of the trajectory and BSS shows the impact parameters.

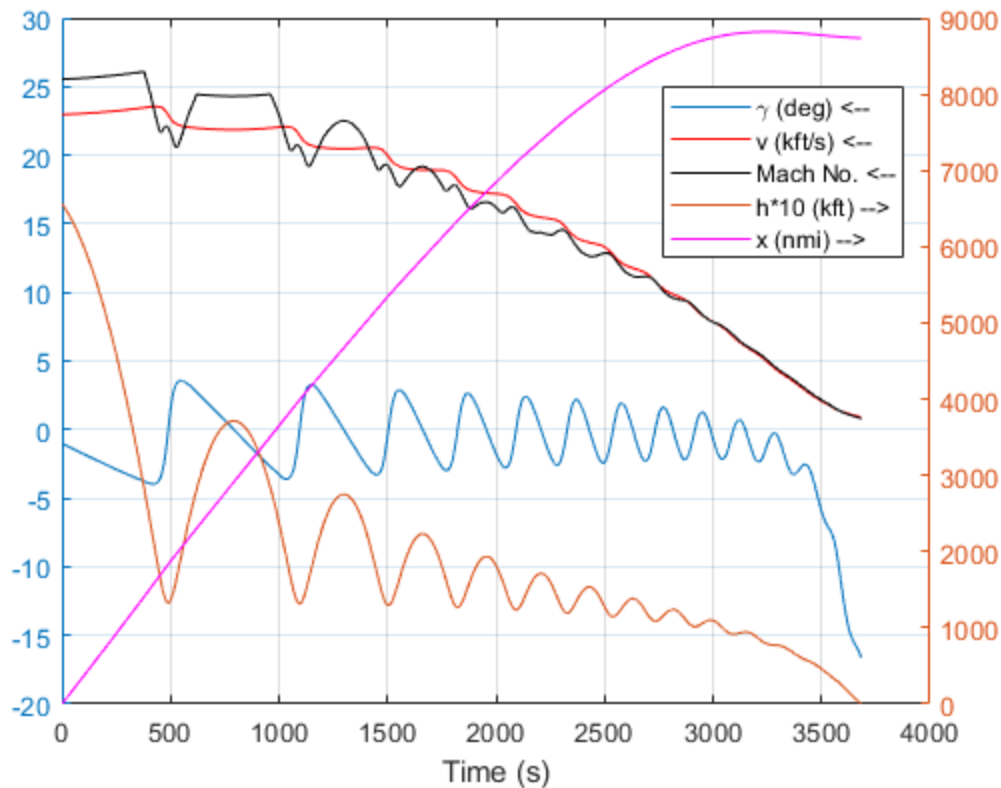


Figure 8.5: Time history of HGV trajectory parameters

Like the RV trajectory, the Mach number has severe changes compared to the velocity due to the change of atmospheric temperature.

Table 8.3: Impact parameters from HGV trajectory

Parameter	Value
Flight Time	61.4 min
Impact Velocity	0.91 kft/s
Impact Mach No.	0.81
Latitude	20.5°S
Longitude	61.4°E
Range	8,736 nmi

The ground track of the HGV trajectory is shown in Figure 8.6. The color of the line corresponds to the maneuvers that vehicle performs. The bank angle of the HGV for the blue, black, and red lines are 0, -10, and 20 degrees respectively. The dotted magenta line shows the

trajectory of the glider if no maneuvers were performed. This trajectory had a total range of 9688 nmi which shows that the HGV can meet the objective RFP requirement.

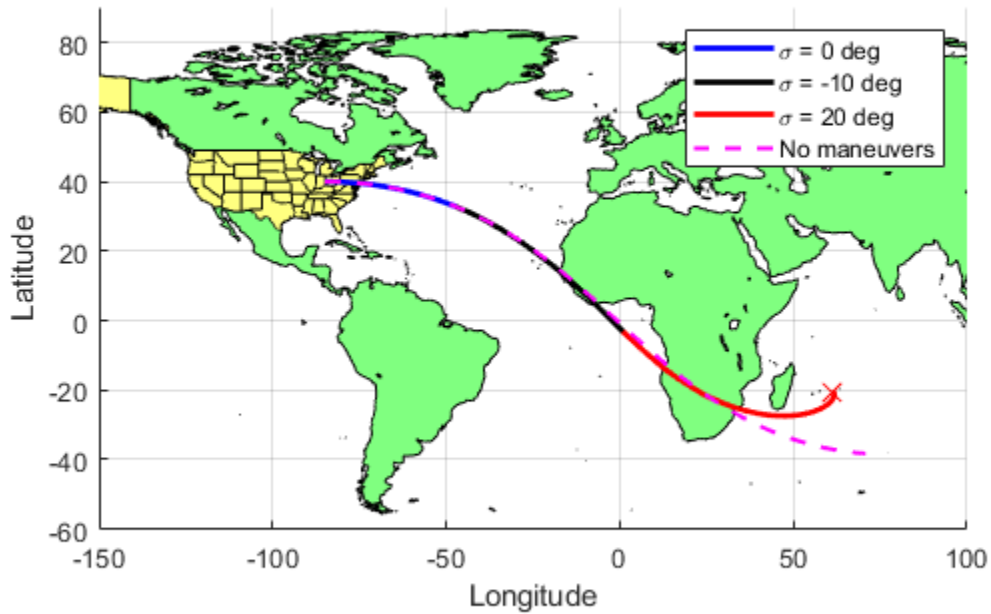


Figure 8.6: Ground track of the HGV trajectory

9 System Level Considerations

9.1 Operations

The overall system is designed to constantly be at a stance of readiness for activation at any notice. In the event that the system be activated, launch orders are delivered from the president and received by the missile crew located at specific launch facilities. The on-site crew then begins a procedure to initiate launch, starting by obtaining access to a locked safe where inside they can get ahold of a sealed-authentication system (SAS). The crew then compares the SAS codes from the launch orders to that in the safe. This then allows them to move forward and begin the launch sequence. The launch sequence is finalized when two crew members synchronously turn a key launching the missile from the silo. The total time elapsed in this process is roughly five minutes. [27]

9.2 System Maintenance

A key requirement for the system is to be without maintenance for at least 20 years. To achieve this, the system is designed with specialized inspection teams that work both independently and collaboratively to maintain system readiness and capabilities. There are four teams comprised of specific tasks. The electro-mechanical team is tasked with maintaining all security systems at the launch facilities and launch sites. They also focus on ensuring command and control communication is always online, as well as inspecting all power systems and back-up power system supplies. The missile maintenance team works hands on in the launch tube checking and maintaining the missiles umbilical system, guidance system and warheads. They service all ignition cabling, explosive ordinances, and the missile suspension system. They inspect the launcher door to maintain healthy operation. The missile handling team is tasked with overseeing all the shipping and receiving of missiles, as well the transportation of missiles to the launch sites.

They install or remove missile stages when necessary with critical attention to the protection of the missile. The last team is the facilities maintenance team which is tasked with monitoring specific temperatures and humidity within the launch control centers, facilities and sites. They ensure primary and secondary power supply from the local commercial grid and the back-up generators. They are a major support for corrosion control teams with a focus on vehicle and the surround systems overall health. [3] These teams upkeep the day to day needs and inspection of the entire system, which ensures it stays at a ready stance, always capable and healthy to be activated in a moment's notice.

9.3 End of Mission Concepts

When the system comes to its end of mission, several considerations are made. The system will undergo a comprehensive maintenance overhaul. The main task to be handled is the disposal of the nuclear warheads. They are transported to Pantex Plant in Carson County, Texas. Pantex Plant is one of six production facilities in the National Nuclear Security Administration (NNSA) where they dismantle nuclear weapons and reuse various components for other purposes. [28] The nuclear material is then put in safe and secure storage. Another major task is the engine disposal. Motors will be transported to Hill Air Force Base in Utah where they can be inspected for reusability. Any healthy motors can be used for testing or applied to new mission designs for new purposes. Any unhealthy or unwanted motors are sent to their Oasis compound where the ICBM motors are disposed of in accordance with the START treaty. [29] These practices assure adherence to standard engineering practices for health, safety, and environmental impact.

9.4 Manufacturing

Stripe Aerospace analyzed all defined components to discover the best method for manufacturing. The manufacturing plan can be seen in Figure 9.1 Figure 9.1: Manufacturing Plan below:

Component	Process
1 st Stage Motor	Custom purchase from Northrop Grumman
2 nd /3 rd Stage Engine	Custom purchase from Aerojet Rocketdyne
2 nd /3 rd Stage Skirt 2 nd /3 rd Stage Thrust Structure 2 nd /3 rd Stage Bulkhead	M.I.H. Aluminum honeycomb
Tanks	M.I.H. Rolled waffle pattern aluminum with friction-stir welded longitudinal seams
Payload Attachment Fitting	Custom purchase from Lockheed Martin
Fairing	Custom purchase from RUAG Space
Post-Boost Vehicle	Custom purchase from Boeing
Re-entry Vehicle	Custom Purchase from AAE Aerospace
Hypersonic Glide Vehicle	Custom purchase from Raytheon

Figure 9.1: Manufacturing Plan

Items such as the stage skirts, stage thrust structures, stage bulkhead, and tank will be made in house (M.I.H.) using patterned aluminum material. The other items will be custom purchased from the companies Stripe Aerospace chose as those chosen to have the most experience and highest quality product.

9.5 Reliability/Redundancy Analysis

The desired reliability for the overall system was decided to be at least 90%. The three types of failure assessed were infant mortality (poor design/manufacturing/coding), environmental overload (storage transportation/launch platform integration), and the reliability of individual parts. The first analysis method for these were key part reliability analysis, in which individual parts were analyzed and derived subsystems were assessed as functions of those key parts. The second analysis method was analyzing general subsystems, which was done so by following an outline provided by [30].

When looking at key part reliability, the components were analyzed as either parallel or series components and assessed as ‘k-out-of-n’ systems, meaning that the system works if k out of

the n components work. The equations below were used to determine individual and system reliability can be seen below:

$$R_{series} = R_1 \times R_2 \times R_3 \times \dots \times R_N \quad (9.1)$$

$$R_{parallel} = 1 - (1 - R_1)(1 - R_2) \quad (9.2)$$

$$R_s = \sum_{j=k}^n \binom{n}{j} R^j (1 - R)^{n-j} \triangleq \sum_{j=k}^n P(j), \quad (9.3)$$

$$P(j) = \binom{n}{j} R^j (1 - R)^{n-j}, \quad (9.4)$$

$$\binom{n}{j} = {}_n C_j = \frac{n!}{j!(n-j)!} \quad (9.5)$$

Table 9.1 below shows the key parts assessed for the vehicle, and their corresponding system reliability:

Table 9.1: Key part reliability analysis

Component	Associated Risk	Individual Reliability	Redundancy	System Reliability
Stage 1 (solid)				
Ignitor	Failure to ignite, damage to motor	80%	3	99.20%
Engine Seals	Failure to seal, releasing hot gas & dropping engine performance	97.75%	2	99.95%
Propellant	Absorbing moisture, decomposition	100%	1	100%
Stages 2 & 3 (liquid stages)				
Ignitor	Failure to ignite, damage to injector	80%	3	99.20%
Propellant	Decomposition	100%	1	100%
Pumps	Seal failure	98%	1	98%
Injector (12 holes)	Clogged orifices, acoustic modes on injector face	100%	1	99.99%
Engine Seals	Failure to seal, releasing hot gas & dropping engine performance	97.75%	2	99.95%

Valve System	Clogged valves, broken valves	98%	2	99.96%
Structural Considerations				
Stage Separation Apparatus	Not all explosives bolts go off	99%	2	99.99%
Payload Attachment (shock absorbers)	Potentially damaging shocks	85%	2	97.75%
Payload Release System	Payload fails to deploy	93%	2	99.51%
Pump Seals	Pump failure causes loss in pressure and performance	95%	2	99.75%
Gimbal System	loss of control, high vibrations, lock up	98%	1	98%
Guidance Navigation and Control				
Celestial navigation	Loss of signal	90%	2	99.00%
IMU		90%	2	99.00%
GPS (payload)		90%	2	99.00%

From the individual parts assessed above, some of the derived systems that were analyzed are the following, as seen in Table 9.2, it should be noted there are many more subsystems to be assessed for an accurate representation of the system reliability, however due to lack of time only the following were closely analyzed:

Table 9.2: Derived subsystem reliability

System Reliability Analysis		
Type of system	Component involved	R_{total}
Parallel:	ignitor/pump	99.97%
	IMU/GPS	99.95%
Series:	pump/valve/injectors	97.94%
	thrust structure/stage separation apparatus	92.86%
	IMU/Gimbal System	92.86%
	Payload shock absorbers/payload release apparatus	90.91%

Analysis from the second analysis method, as provided by [30], can be seen in Table 9.3 below:

Table 9.3: General subsystem reliability analysis

Subsystem	System Reliability
Infant Mortality	
Structure	1
Inertial guidance	0.995
Power supply	1
Propulsion	0.985
Fuze	0.9999
Environmental Overload	
Storage	1
Transportation	0.9995
Launch Platform Integ.	0.9995
Flight	0.9995
System Overall Reliability	
Total	97.9%

After performing the analysis, as seen above, the estimated vehicle reliability is 97.9%.

9.6 Cost Analysis

Cost analysis was performed using two different methods. The first method was the *Space Planners Guide* by the United States Air Force [31]. This method for analysis was best for estimating programmatic costs such as operational production, vehicle operations, and ground equipment production. The method used empirical data to estimate these costs to compare the design too. Some of the considerations taken into account with this method is hardware design/development/support, ground and flight test hardware, development test operations, launch vehicle facilities, ground equipment production, operational production, and vehicle operations. Its final cost estimate would be in 1965 US dollars that would need to be adjusted for inflation using the equation below:

$$US\ Dollar\ 2019 = US\ Dollar\ 1965 * (8.07) [32]$$

This method is not very accurate as the estimates are taken by reading graphs; the graphs are small with a wide range in values so estimates can easily be skewed by a few thousand or million without proper software. This inaccuracy is what creates the need for a second estimation.

The second method for analyzing cost came from using the TRANSCOST 8.1 analysis method [33]. This method had far more up to date numbers for estimating the cost of engineering and production of the hardware of the missile. It is performed using the same mass estimation graphs as the *Space Planner Guide* but with more data points that come from a more relevant era its yielding values are more believable.

Table 9.4: Cost Estimation Breakdown

Space Planners Guide Cost Estimate		
Total DT&E Cost	1283.3	M
Total Facilities	3116.4	M
Total AGE Production	720.0	M
Total Hardware Production	1521.5	M
Total Operations	6374.2	M
Total LV System Program	13015.3	M
Total (1965)	13.0	B
Total (2019)	104.7	B

When combining these two cost estimation methods, the result was a total program cost of \$13.0 billion in 1965 dollars or using the equation above, \$104.7 billion in 2019 US dollars.

The optional hypersonic glide vehicle is estimated to cost an additional total of \$7.2 billion 2019 US dollars. This estimate comes from this price included the engineering and production cost and is not included in the previous total program cost, as this is an optional upgrade. If included, the new program total cost would be \$111.9 billion 2019 US dollars. This falls between the USAF estimate of \$62 billion and the Pentagon estimate of \$85 to \$140 billion [34].

9.7 Program Timeline

The team of systems engineers at Stripe Aerospace has done their best in planning and estimating a timeline for the strategic missile program. Below, Figure 9.2, is based on a start date of October 2020 with a goal of Initial Operational Capabilities on December 2029.

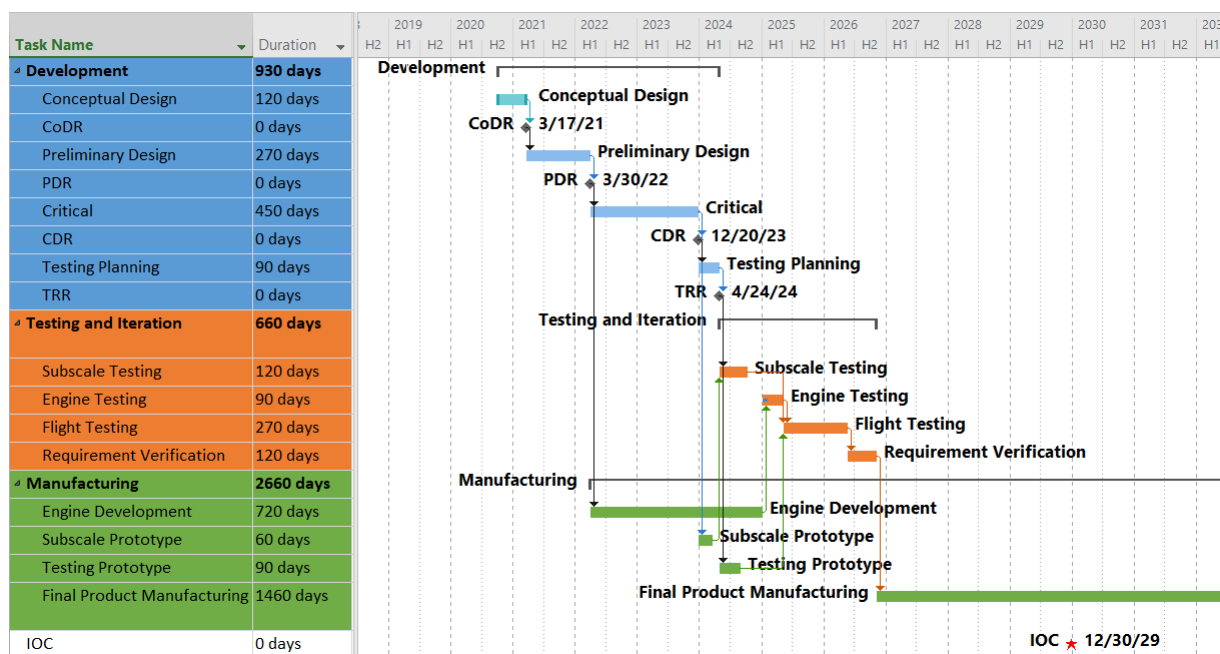


Figure 9.2: Program Timeline

The timeline is broken up into three sections detailing the development, testing and iteration, and manufacturing phases of the program. The first subscale test will happen in early 2024 with the final test flight happening mid-2026. Final product manufacturing will start in late 2026.

10 Compliance Matrix

The design of the missile system proposed by Project Fenrir can be shown to be compliant with RFP requirements in Table 10.1.

Table 10.1: Compliance Matrix

Req. No.	Requirement	Compliance	Comment
T0.0-1	The weapon system must be capable of carrying a minimum of two 1000 lb _m payload with a 22 in diameter and 80 in length.	Yes	Payload is incorporated into inboard profile, mass estimates, and shown to fit inside CAD models.
T0.0-2	The missile system must be able to engage targets of interest from a maximum threshold distance of 7000 nmi, with an objective range of 10000 nmi.	Yes	Trajectory analysis shows that the missile is capable of reaching the 10,000 nmi objective range.
T0.0-3	The missile system must be capable of storage for up to 20 years without maintenance.	Yes	Maintenance needs are satisfied by selecting storable propellants (solids and storable liquids).
T0.0-4	The CEP of each independent payload shall be a maximum of 100 ft (objective), 150 ft (threshold) with a footprint of 100 nmi between impact points of the payloads.	Yes	Monte Carlo analysis has been performed with a 3DOF reentry trajectory model. Tolerances for reentry initial conditions are defined to meet CEP requirement.
T0.0-5	The weapon system shall use an IMU and celestial navigation to guide to the separation point, and each independently guided payload shall be GPS guided, with a backup guidance system in case of GPS denial.	Yes	A block diagram of the control system incorporates these components.
T0.0-6	The missile shall deploy payloads at an objective flight time of 60 minutes, threshold of 90 minutes.	Yes	Trajectory analysis shows that the payloads will detach from the vehicle before 90 minutes.
M0.0-1	Project development shall begin no later than October 2020, with IOC occurring no later than December 2029.	Yes	Gantt chart has been laid out for the program to meet deadlines.

T0.0-7	The vehicle shall be launched from either a fixed location using existing Minuteman-III silos or a mobile platform using a truck or train car.	Yes	Silo dimensions have been determined and existing architectures have been designed to fit inside silos. Mobile launch platform has been determined to be unfeasible.
C0.0-1	The cost estimate shall include the cost of the weapon system, and silo or launcher costs. Costs for any proposed modifications to existing launch equipment or development of new such equipment must be included.	Yes	Cost analysis of the system has been performed using the 1965 Air Force Space Planner's Guide and TRANSCOST 8.1. Adjustments have been made for inflation to 2019.
C0.0-2	System shall possess 450 operational missiles and 5 missiles for testing purposes with 10 missiles for each of the 45 launcher sites.	Yes	Cost has been estimated for 450 production missiles and an additional 5 units for testing.
M0.0-2	Design shall adhere to standard engineering practices for health, safety and environmental impact. Consideration to current treaties and public perception shall be addressed.	Yes	Safety and handling practices for propellants have been considered. End of mission disposal concepts have been defined. Current treaties have been researched and addressed.

11 Summary and Conclusions

A proposed missile system has been designed to replace the Minuteman-III ICBMs and improve upon the capabilities. From the analysis shown in this report, the system is proven to meet all RFP requirements. The missile is capable of deploying two independent RVs to targets 10,000 nmi away under the 90 minute threshold. Storable propellants were chosen so that missile could be safely stored in a silo for 20 years without no maintenance. A CEP of 130 ft was obtained for certain tolerances on the initial conditions of the reentry vehicle which led to defining a control system for thrust vectoring and the post boost vehicle in order to meet those tolerances. Other components of the system were defined such as human interaction, considerations of treaties and environmental impact, manufacturing, etc. After creating a preliminary design of the missile and considering the entirety of the system, the total cost estimate for the system became around \$111.9 billion dollars.

The largest risk with this system is the use of liquid propellants due to past worries of handling, storage, and reliability. An additional concern comes from the longer development time of new liquid rocket engines which may cause cost overruns with the schedule. Analysis has shown that JP-10 and 98% hydrogen peroxide has no issues being stored for at least 20 years. Working with an industry expert on hydrogen peroxide has shown that hydrogen peroxide can be a reliable oxidizer. The hazards of MMH and N₂O₄ may not be as severe now as they were decades ago when the technology to handle them was still new. However, if those propellants prove to become troublesome with further research and design, the stage could be eliminated in favor of having a larger JP-10 and hydrogen peroxide stage. The schedule laid out to meet IOC gives a few years of slack before the 2029 deadline so that any mishaps during development and testing can be fixed.

An additional recommendation for further research is the use of gel propellant as it combines the best features of solid and liquid propellants.

With the proposed design at its current state, more iteration can be performed to further optimize the system. Given that the trajectory analysis shows that over 10,000 nmi is achieved, the vehicle should be resized to meet the range of proposed range of 9,265 nmi. This will somewhat reduce the size and cost of the vehicle and still allow for any major landmass to be targeted.

The hypersonic glide vehicle is a more innovative method of delivering a warhead to a target. A significant amount of effort by the team was put into understanding the design and analysis for the HGV. From the trajectory analysis done, it shows promise by meeting the range requirement. However, the viability of the HGV is still unclear since the technology level still requires much more development that may not fit the schedule laid out to meet IOC. Since the HGV is not required at all to meet RFP requirements, further design work on it should not be considered. Instead, if desired, the missile can be analyzed to accommodate an HGV designed by another source so that the vehicle design can be reused for other purposes.

References

- [1] J. Lewis, "Return of the Hard Mobile Launcher," Arms Control Wonk, 14 June 2012. [Online]. Available: <https://www.armscontrolwonk.com/archive/205381/return-of-the-hard-mobile-launcher/>.
- [2] R. Beckhusen, "American Mobile Nuclear Missile Launchers Is a Really Bad Idea," The National Interest, 3 October 2017. [Online]. Available: <https://nationalinterest.org/blog/the-buzz/american-mobile-nuclear-missile-launchers-really-bad-idea-22579>.
- [3] D. Fields, "Minuteman Missile a Tribute To The ICBM Program," NoteTab Pro, 2011. [Online]. Available: <https://minutemanmissile.com/about.html>.
- [4] J. F. Ahearne, "Effects of Nuclear Earth-Penetrator and Other Weapons," National Academies Press, Washington D.C, 2005.
- [5] C. Young, "Penetration Equations," Sandia National Laboratories, Albuquerque, 1997.
- [6] U. Academy, Astronautics 332 Course Text (Volume 1), Colorado: Department of Astronautics and Computer Science, 1980.
- [7] D. Edberg and W. Costa, Elements of Space Launch Vehicle Design, Cognella, 2018.
- [8] M. Ventura, E. Wernimont, S. Heister and S. Yuan, "Rocket Grade Hydrogen Peroxide (RGHP) for use in Propulsion and Power Devices-Historical Discussion of Hazards," in *43rd AIAA/ASME/SAE/ASEE Joint Propulsion Conference & Exhibit*, 2007.
- [9] T. Brown, Wright-Patterson AFB, 9 September 2011. [Online]. Available: <https://www.wpafb.af.mil/News/Article-Display/Article/399775/study-saves-resources-by-extending-storage-life-of-jp-10-fuel/>. [Accessed 1 March 2019].

- [10] D. K. Huzel and D. H. Huang, *Modern Engineering for Design of Liquid-Propellant Rocket Engines*, American Institute of Aeronautics and Astronautics, 1992.
- [11] R. W. Humble, G. N. Henry and W. J. Larson, *Space Propulsion Analysis and Design*, McGraw-Hill, Inc., 1995.
- [12] D. H. Mitchell, "FLIGHT SEPARATION MECHANISMS," National Aeronautics and Space Administration, Langley, 1970.
- [13] H. Ashley, *Engineering Analysis of Flight Vehicles*, Mineola: Dover Publications, Inc., 1974.
- [14] NOAA, NASA and USAF, "U.S. Standard Atmosphere, 1976," National Aeronautics and Space Administration, Washington, DC, 1976.
- [15] S. Josselyn and I. M. Ross, "Rapid Verification Method for the Trajectory Optimization of Reentry Vehicles," *Journal of Guidance, Controls, and Dynamics*, vol. 26, no. 3, pp. 505-508, 2003.
- [16] W. J. Larson and L. K. Pranke, "Fig. 10-6. Newtonian Hypersonic Aerodynamics," in *Human Spaceflight: Mission Analysis and Design*, McGraw-Hill, 199, p. 288.
- [17] J. D. Anderson, *Hypersonic and High-Temperature Gas Dynamics*, Reston: American Institute of Aeronautics and Astronautics, 2006.
- [18] L. Gronlund and D. C. Wright, "Depressed Trajectory SLBMs: A Technical Evaluation and Arms Control Possibilities," *Science & Global Security*, vol. 3, pp. 101-159, 1992.
- [19] F. J. Regan and S. M. Anandakrishnan, *Dynamics of Atmospheric Re-Entry*, Washington, DC: American Institute of Aeronautics and Astronautics, 1993.

- [20] "Metallic Materials Properties Development and Standardization," *MMPDS*, vol. 11, p. 2426, 2016.
- [21] R. H. Speier, G. Nacouzi, C. A. Lee and R. M. Moore, "Hypersonic Missile Nonproliferation: Hindering the Spread of a New Class of Weapons," RAND, 2017.
- [22] K. G. Bowcutt, J. D. Anderson, Jr. and D. Capriotti, "Viscous Optimized Hypersonic Waveriders," in *AIAA 25th Aerospace Sciences Meeting*, Reno, 1987.
- [23] S. Corda and J. D. Anderson Jr., "Viscous Optimized Hypersonic Waveriders Designed from Axisymmetric Flow Fields," in *AIAA 26th Aerospace Sciences Meeting*, Reno, 1988.
- [24] T.-t. Zhang, W. Huang, S.-b. Li and Z.-g. Wang, "A Novel Design Technique of Hypersonic Gliding Vehicle," in *7th European Conference for Aeronautics and Space Sciences*, 2017.
- [25] D. Feng, L. Jun, J. Liang and L. Shi-bin, "Comparison between methods of generation of waveriders derived from streamline tracing and simplified method," *Applied Mechanics and Materials*, vol. 390, pp. 134-140, 2013.
- [26] J. M. Acton, "Hypersonic Boost-Glide Weapons," *Science & Global Security*, vol. 23, pp. 191-219, 2015.
- [27] *Titan Missile Museum Tour*, Sahuarita, 2019.
- [28] "About Pantex," Pantex Plant, Carson County, 2019.
- [29] "Government accountability Office," [Online]. Available: <https://www.gao.gov/assets/690/687571.pdf> .
- [30] E. L. Fleeman, *Missile Design and System Engineering*, Reston: American Institute of Aeronautics and Astronautics, 2012.

- [31] United States Air Force Systems Command, Space Planners Guide, Washington, D.C.: U.S. G.P.O., 1965.
- [32] "\$1 in 1965 → 2019 | Inflation Calculator. U.S. Official Inflation Data," Alioth Finance, [Online]. Available: <https://www.officialdata.org/us/inflation/1965?amount=1>.
- [33] D. E. Kölle, "Handbook of cost engineering for space transportation systems : including TRANSCOST 8.1 statistical-analytical model for cost estimation and economical optimization of launch vehicles," Ottobrun, Germany: TransCostSystems, 2010.
- [34] J. Daniels, "Competition to replace US nuclear missiles is down to 2 companies, but uncertainties remain," 22 August 2017. [Online]. Available: <https://www.cnbc.com/2017/08/22/competition-to-replace-us-nuclear-missiles-is-down-to-2-companies.html>.